Turbulent flow topology in supersonic boundary layer with wall heat transfer

Mostafa Safdari Shadloo, Sushank Sharma, A. Hadjadj

Mostafa Safdari Shadloo, Sushank Sharma, A. Hadjadj. Turbulent flow topology in supersonic boundary layer with wall heat transfer. International Journal of Heat and Fluid Flow, 2019, 78, pp.108430. ⟨10.1016/j.ijheatfluidflow.2019.108430⟩. ⟨hal-02189352⟩

Turbulent Flow Topology in Supersonic Boundary Layer with Wall Heat Transfer

S. Sharma, M. S. Shadloo[1] and A. Hadjadj

CORIA-UMR 6614, CNRS-University, INSA of Rouen and Normandie University, France

---

Abstract

Direct numerical simulations (DNS) are performed for the supersonic boundary layers (SBLs) with a free-stream Mach number $M_\infty = 2.2$. Different cases including the adiabatic and the isothermal (cooled and heated) walls are investigated. The laminar boundary layer is excited by means of a blowing and suction strip with single-frequency and multiple spanwise wave-numbers. The incoming laminar flow is strongly perturbed with a perturbation intensity of 2.4% of the free-stream velocity to obtain the turbulent boundary layer. In the fully developed turbulent regions, the joint probability density function (JPDF) distribution and the covariance integrands' analyses of different parameters are performed to find out the contribution of various physical mechanisms towards different transfer processes. The results reveal that behavior of the turbulent shear stress is similar to its incompressible counterpart and the wall-temperature impacts are dominant in the buffer layer region (at $y^+ = 10$). The inclination angles of coherent structures show variations arising from the wall-temperature in both the buffer-layer and the

---

[1] Email for correspondance: msshadloo@coria.fr

Preprint submitted to International Journal of Heat and Fluid Flow *May 6, 2019*

log region. The covariance integrands' analyses of different components of the heat flux reveal the dominance of a different transfer process in case of the cooled wall, and as a result of this difference, the cooled wall acts as a heat sink.

Keywords: Supersonic boundary layer, Turbulent flow, Direct numerical simulation (DNS), Joint Probability Distribution Function (JPDF) distribution, Covariance integrand analysis

---

1. Introduction

An increasing focus towards the improvement in the designs of the supersonic aircraft, calls for a better understanding of the high-speed flows. Various other applications such as the flow through a supersonic propulsive nozzle [1], demand for better characterization of the supersonic turbulent boundary layers. Due to the complexity posed by the compressibility effects in case of the high-speed flows, it therefore becomes necessary to explore the implications of different physical parameters such as the surface temperature on the flow itself [2].

The scientific community is trying to characterize the turbulent flows from a very long period of time. The study performed by Theodorsen [3] brings out the importance of the coherent structures in case of the incompressible turbulent wall-bounded flows. Their results shed light on the fact that these structures are responsible for low-momentum fluid transport and Reynolds shear-stress production. The morphology of these structures were experimentally verified by Head and Bandyopadhyay [4]. The investigation presented in [5] suggests that in the turbulent boundary layer, the asymmetric one-legged hairpin vortex is the most-probable shape of the coherent structures. Later on, the numerical study performed by Wu and Moin [6] stated that the forests of hairpin vortices dominate the turbulent boundary layer. Experimentally, the events of ejections and sweeps which are responsible for Reynolds shear-stress production were visualized by Corino and Brodkey [7]. Wallace et al. [8] quantified the turbulent processes and provided further insight about Reynolds stress production in the near-wall region for the incompressible turbulent channel flows. Their results reveled that ejections and sweeps together contribute more than 100% to the Reynolds stress, and the additional stress was countered by other contributing factors named interactions.

For the incompressible turbulent channel flows, Wallace and Brodkey [9] performed the joint probability density distribution function (JPDF) and the covariance integrands' analyses for the streamwise and wall-normal velocity fluctuations in order to find out the contribution of different transport processes towards the Reynolds shear-stress. Their results suggest that when moving from the near wall-region i.e. $y^+ = 5$ to the end of the log region, different physical phenomena dominate the transfer processes. They also showed that the most-probable velocity pairs did not have the largest contribution towards the shear-stress. Major contribution of ejections towards the Reynolds shear stress was also reported by the experimental investigation of Willmarth and Lu [10]. The results presented by Ong and Wallace [11] highlighted the ability of the JPDF and covariance analyses in determining the topology of the turbulent flows. The results of this study helped in determining the most probable angles of inclination of the vorticity filaments using the covariance integrands' analyses. The events of vortex stretching and compression were also discussed in detail. It was found that the average stretching of the filaments was greater than compression at all of the considered locations [11]. Direct numerical simulations (DNS) of Le et al. [12] investigated the changes in three-dimensional turbulent boundary layer by employing a combination of different statistical and visualization methods. Their results uncovered that mean three-dimensionality was responsible for breaking up the symmetry and alignment of the near-wall coherent structures disrupting their self-sustaining mechanisms, and resulting in the reduction of the turbulent kinetic energy.

Fewer investigations have been performed so-far for the compressible turbulent boundary layers. For low Mach number turbulent boundary layers, the DNS results of Bechlars and Sandberg [13] found the potential backscatter mechanism for the transfer of the kinetic energy from smaller scales to the larger scales. The effects on the first three invariants of the velocity gradient tensor with wall-normal distance for weakly compressible flow are studied by [14]. The experimental database available for the compressible problems is scarce due to the difficulty in measurements. The experimental investigation of Spina et al. [15] revealed that the compressibility has little impact on the statistical properties of the flow. One of the first investigations reported by Morkovin [16] suggests that the effects of compressibility on turbulence are due to the variations of the thermodynamic properties across the boundary layer. The experimental data also confirms that the supersonic boundary layers bear close similarities to the incompressible ones [17, 18]. Li and Xi-Yun [18] have reported that the angles of inclination of the vortical structures with the streamwise direction increases from sub-layer to buffer layer and then decreases from the buffer layer to the wake region. Maeder et al. [19], Pirozzoli et al. [20] have investigated the structural characteristics of the supersonic turbulence and found the presence of the organized motions in the outer layer. The study presented in [21] tried to quantitatively characterize the statistical features of the coherent structures for the case of turbulent supersonic boundary layer and found that the inner layer was mostly populated by the quasi-streamwise vortices while the outer layer (including the log and the wake regions) was populated by different types of structures such as the hairpin vortices and the hairpin packets.

The careful examination of the existing scientific literature revels that the studies pertaining to the effects of wall heat-transfer on turbulent flow topology for the compressible supersonic boundary layer are scarce (almost none for the heated wall). The study investigating the supersonic cooled turbulent channel flows in [22] deals with the effects of compressibility on the pressure-strain correlation and the dissipation rate tensors in the Reynolds stress budgets. The results of this study revealed that the fluctuations conditioned on ejections and sweeps in the wall-layer were instructive, and showed that the positive temperature fluctuations were mainly due to sweeps in case of the cooled wall. Moreover, the comparison with the incompressible flow data underlined that the compressibility effects persisted in the wall-layer only. Relevant statistical properties of the compressible turbulent flows (including the heated wall) are assessed in [23]. This study found that the Morkovin's hypothesis was neither valid for the heated walls nor for the cooled walls. The analysis of the turbulent kinetic energy budget showed that the dilatational to solenoidal dissipation ratio increases/decreases with heating/cooling of the wall. Later on, Trettel and Larsson [24] proposed the transformations of the velocity and the wall-coordinate simultaneously for the supersonic isothermal turbulent channel flows and the turbulent boundary layers, relating the compressible mean velocity profile at any given Mach number. For low-Mach number heated channel flows, Patel et al. [25] found that the van Driest transformed mean temperature profiles of variable property cases collapsed with the constant property cases if the semilocal Reynolds number and the local Prandtl number distributions are constant across the channel. Chu et al. [26] studied the effects of wall temperature on the orientation of the vortical structures and other statistical properties like Morkovin's scaling. It was found that with increasing wall-temperature, the spanwise distance between the legs of the hairpin vortex increased, the mean swirling strength and the angle of the vorticity filament with the wall also increased in the inner layer. However, the statistical properties of the vortical structures were nearly insensitive to the wall temperature in the outer layer. Moreover, they also put forward a new criteria for better characterizing the angles of inclination of the vortical structures. Other works characterized the factors influencing the transition scenarios for the compressible supersonic flows [27, 28, 29].

For the supersonic boundary layers, it is important to address the impacts of wall-heating and cooling on the arrangement and the orientation of the vortical structures, and the heat-transfer mechanisms, which are the fundamental and still open questions for the community. In this study, the JPDF and the covariance integrands' analyses are utilized to unravel the physical mechanisms responsible for the heat-transfer in the streamwise and the wall-normal directions. Various quadrant analyses have been put forward to find out the most-significant and contributing transfer process responsible for the turbulent shear stress, the vortical structures' orientation and the turbulent heat-flux.

This paper is structured as follows: the governing equations and details of the computational setup including the boundary conditions are given in §2, followed by the description of the turbulent boundary layer in §3. Then a detailed discussion about the turbulent shear stress, topology of the coherent structures and different components of the turbulent heat-transfer is presented in §4.1, §4.2 and §4.3, respectively. The conclusions of the paper are presented in §5.

2. Description of the numerical setup

2.1. Governing equations

The motion of a Newtonian fluid is governed by the set of equations known as the $Navier-Stokes\ equations$ (NSE) comprising of the equations of conservation of mass, momentum and total energy. The NSE are non-dimensionalized using the free-stream quantities and the boundary layer thickness at the inlet δ^*_{in} as the reference length:

$$\frac{\partial \rho}{\partial t} + \frac{\partial \rho u_j}{\partial x_j} = 0, \tag{1}$$

$$\frac{\partial \rho u_i}{\partial t} + \frac{\partial \rho u_i u_j}{\partial x_j} = -\frac{\partial p}{\partial x_i} + \frac{\partial \tau_{ij}}{\partial x_j}, \tag{2}$$

$$\frac{\partial \rho E}{\partial t} + \frac{\partial (\rho E + p) u_i}{\partial x_i} = -\frac{\partial q_i}{\partial x_i} + \frac{\partial u_i \tau_{ij}}{\partial x_j}, \tag{3}$$

where, density $\rho = \rho^*/\rho^*_\infty$, velocity $u = u^*/u^*_\infty$, time $t = t^* \times u^*_\infty/\delta^*_{in}$, pressure $p = p^*/(\rho^*_\infty u^{*2}_\infty)$ and energy $E = E^*/u^{*2}_\infty$. Throughout this paper, the free-stream quantities are marked by the subscript ∞ and the dimensional quantities are marked by the asterisk superscript $(^*)$.

τ being the symmetric viscous stress tensor, which is given by:

$$\tau_{ij} = \frac{\mu}{Re}\left(\frac{\partial u_j}{\partial x_i} + \frac{\partial u_i}{\partial x_j} - \frac{2}{3}\frac{\partial u_k}{\partial x_k}\delta_{ij}\right). \tag{4}$$

where, viscosity $\mu = \mu^*/\mu^*_\infty$, Reynolds number $Re = \rho^*_\infty u^*_\infty \delta^*_{in}/\mu^*_\infty$ and δ_{ij} is the Kronecker delta. The pressure and the heat-flux are computed using the equation of state and the Fourier law of heat conduction respectively:

$$p = (\gamma - 1)\left(\rho E - \frac{1}{2}\rho u_i u_i\right) = \frac{1}{\gamma M^2_\infty}\rho T, \tag{5}$$

and

$$q = \frac{-\mu}{(\gamma - 1)M^2_\infty Re Pr}\frac{\partial T}{\partial x_j}. \tag{6}$$

with temperature $T = T^*/T^*_\infty$, constant specific heat ration $\gamma = 1.4$ and Mach number $M_\infty = u^*_\infty/\sqrt{\gamma R^* T^*_\infty}$ with gas constant $R^* = 287 J/K kg^{-1}$ and Prandtl number $Pr = 0.72$.

The Sutherland's law has been used to calculate the dynamic viscosity:

$$\mu^*(T^*) = \frac{C^*_1 T^{*3/2}}{T^* + S^*}, \tag{7}$$

where, $S^* = 110.4$ K is Sutherland's temperature for air and C^*_1 is a constant, $1.458 \times 10^{-6}\ kg/ms\sqrt{K}$ which can be written as:

$$C^*_1 = \frac{\mu^*_r}{T^{*3/2}_r}(T^*_r + S^*), \tag{8}$$

where μ_r^* is the reference dynamic viscosity of the air, 1.716×10^{-5} kg/ms at the reference temperature, T_r^* of 273.15 K. The subscript r refers to the reference values.

2.2. Numerical solver

We have utilized a well validated DNS - LES numerical solver named CHOC-WAVES to solve the three-dimensional, compressible, unsteady NSE for perfect gases. This solver discretizes the convective fluxes by a hybrid conservative sixth-order central scheme with fifth-order Weighted Essential Non-Oscillatory (WENO) scheme [30, 31]. Convective terms are splitted in a skew-symmetric form to minimize the aliasing error and to enforce discrete conservation of the kinetic energy which results in better numerical stability. Approximation of the diffusive terms is done with the fourth or the sixth order formulas, and they are expanded in the Laplacian form. The time integration is performed using the third-order Runge-Kutta (RK-3) scheme. More details on validation can be found in ([32, 33, 34]).

2.3. Problem setup

This study utilizes the supersonic flow over a flat plate with free-stream Mach number $M_\infty = 2.2$, temperature $T_\infty^* = 177$ K, pressure $p_\infty^* = 23796$ Pa and viscosity $\nu_\infty^* = 2.55 \times 10^{-5}$ m^2/s. The choice of the Mach number is based on the fact that at higher Mach numbers, the second mode instabilities or the Mack modes [35] dominate the flow and hence the effects of wall heat-transfer could not be distinguished prominently [27, 28, 29]. The computational domain is free of the shocks generated at the leading edge of the flat-plate because the inlet is placed downstream of the leading edge at

$x^*_{in} = 0.1016$ m with inlet Reynolds number $Re_{x_{in}} = 2.33 \times 10^6$ and unit Reynolds number $Re^*_{unit} = 2.293 \times 10^7/\text{m}$. The length and the height of the domain are $L^*_x = 0.15$ m and $L^*_y = 0.0127$ m respectively. The height of the computational domain is chosen such that the boundary layer thickness towards the end of the domain is approximately one-third of the height of the domain. The spanwise width of the domain is set equal to the fundamental wavelength of the excited mode i.e. $L^*_z = \lambda^*_z = 0.00605$ m corresponding to the most-unstable mode predicted by the Linear stability theory (LST) [27, 28]. Two-point correlations in the spanwise direction are plotted (not shown here) which assure that the periodicity does not affect the generated turbulence. Uniform mesh spacing is used in both the streamwise and the spanwise directions with $N_x = 4096$ and $N_z = 280$ being the number of points in the given directions. However, in the wall-normal direction ($N_y = 150$), points are more concentrated close to the wall in order to resolve the boundary layer. The stretching function in the wall-normal direction is given by:

$$y^* = L^*_y \, \frac{1 + \tanh(\kappa_o y^*)}{\tanh(\kappa_o)}, \tag{9}$$

with, $\kappa_o \approx 3$ being the stretch parameter.

Details about various DNS cases under investigation are enlisted in table 1. In this table, A, C and H stand for the adiabatic, cooled and heated walls respectively. As seen in table 1, constant excitation frequency i.e. $\omega^* = 150$ krad/s (or 23.87 kHz) is chosen for the blowing and suction strip for all the cases which corresponds to the most-unstable frequency according to the LST [27, 28]. Moreover, the perturbation intensity is kept high i.e. 2.4% of the free-stream velocity in order to strongly excite the boundary layer, so that

Table 1: Computational parameters for various test cases. A, C and H stand for the adiabatic, the cooled and the heated walls, respectively. Subscript *min* denotes the wall-normal spacing. Superscript + denotes the quantities in wall-units. I is the disturbance amplitude of blowing and suction ($I = v^*_{wall,max}/u^*_\infty$).

Cases	T^*_w/T^*_{aw}	$I(\%)$	ω^* (krad/s)	Δx^+	Δy^+_{min}	Δz^+
A0[27]	1.00	2.4	150	5.52	0.34	2.85
A	1.00	2.4	150	5.52	0.34	3.26
C	0.75	2.4	150	8.11	0.50	4.78
H	1.50	2.4	150	3.30	0.20	1.95

the turbulent boundary layer exists in the majority of the computational domain ($> 50\%$).

2.3.1. Boundary conditions

Figure 1 represents a schematic the computational domain and the boundary conditions. At the inlet of the domain, the streamwise and the wall-normal velocities, as well as the density profile are set to the laminar Blasius profile, without any disturbance. These profiles are calculated using a dedicated solver to obtain similarity solutions for adiabatic and isothermal compressible laminar boundary layers which utilizes the Illingworth transformation [36, 37]. The boundary layer thickness at the inlet of the domain δ^*_{in} for A, C and H cases are 4.44×10^{-4} m, 3.91×10^{-4} m and 4.86×10^{-4} m respectively. For the adiabatic case, the wall temperature $T^*_w = T^*_{aw}$ (adibatic wall temperature), while for cooled and heated walls the temperature is set as $T^*_w = 0.75\ T^*_{aw}$ and $T^*_w = 1.5\ T^*_{aw}$ respectively, where $T^*_{aw} \approx 1.82\ T^*_\infty$. T^*_{aw}

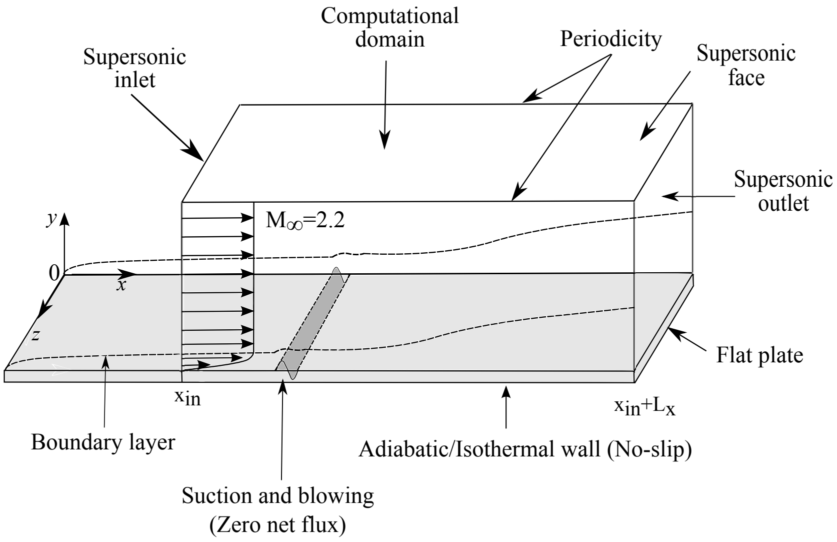

Figure 1: Computational domain and boundary conditions.

is calculated using the recovery factor approximation $Pr^{1/3}$, [36]:

$$T^*_{aw} = T^*_\infty \left(1 + Pr^{1/3} \times \frac{\gamma - 1}{2} \times M^2_\infty\right) \tag{10}$$

Supersonic inflow and outflow boundary conditions are imposed at the inlet (x^*_{in}) and at the outlet ($x^*_{out} = x^*_{in} + L^*_x$) respectively. The side-walls of the domain are periodic and for the upper face of the domain, zero boundary-normal gradient is imposed. No-slip and no-penetration condition is used for at the surface of the wall ($y = 0$), except for the narrow strip of blowing and suction existing between $x^*_a = x^*_{in} + 0.0127$ m to $x^*_b = x^*_{in} + 0.0254$ m. The wall-normal component of the velocity in the blowing and suction strip is prescribed by the single-frequency and multiple-spanwise wavenumber boundary condition given as:

$$v^*(x, y = 0, z, t) = I u^*_\infty \; f(x) \left[\frac{g(z)}{max(g(z))}\right] \left[\frac{h(t)}{max(h(t))}\right], \tag{11}$$

where I is the disturbance amplitude, $f(x), g(z)$ and $h(t)$ are the streamwise, spanwise and time-dependent variations respectively, defined as:

$$f(x) = 4\ \sin\theta(1 - \cos\theta)/\sqrt{27}, \tag{12}$$

$$g(z) = \sum_{l=1}^{l_{max}} Z_l\ \sin(2\pi l(z^*/L_z^* + \phi_l)), \tag{13}$$

$$h(t) = \sum_{m=1}^{m_{max}} T_m\ \sin(\omega^* t^* + \phi_m). \tag{14}$$

Here, ω^* is the fundamental frequency of the induced disturbance, $\theta = 2\pi(x^* - x_a^*)/(x_b^* - x_a^*)$, and ϕ_l and ϕ_m are the random numbers between 0 and 1. The random numbers are generated using the FORTRAN subroutines of RANDOM_NUMBER and RANDOM_SEED which generate the pseudo-random numbers with uniform distribution between 0 and 1. $\sum_{l=1}^{l_{max}} Z_l = 1$, $Z_l = 1.25 Z_{l=1}$, with $l_{max} = 20$ and $\sum_{m=1}^{m_{max}} T_m = 1$, $T_m = 1.25 T_{m=1}$, with $m_{max} = 20$. The above mentioned methodology for generating fully developed turbulent boundary layer is a modified version of the method used by Pirozzoli et al. [20]. This methodology has been used by Shadloo et al. [27] and Shadloo and Hadjadj [28], and their results present good agreement with the turbulent boundary layer results of Shadloo et al. [23] (cf. figures 4 and 8 in [28]).

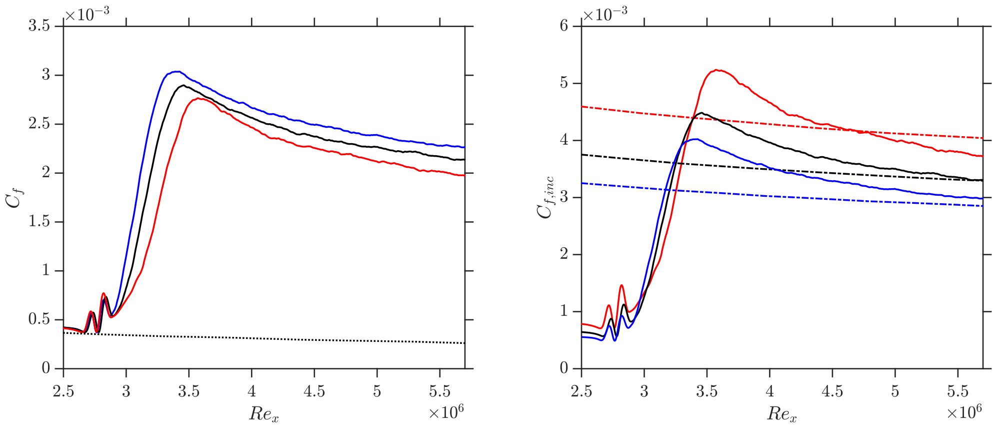

(a)

(b)

Figure 2: Streamwise evolution of (a) compressible, and (b) incompressible skin-friction coefficients as a function of Re_x for cooled (—), adiabatic (—) and heated (—) cases. Here, (·····) is ($C_{f,lam} = 0.664 \times \frac{\sqrt{\rho^*_w \mu^*_w / \rho^*_\infty \mu^*_\infty}}{\sqrt{Re_x}}$) and (—··) is ($C_{f,inc(turb)} = 0.074 \times \sqrt{\frac{\rho^*_{aw}}{\rho^*_w}} \times Re_x^{-0.2}$) lines represent the theoretical curves for the laminar and the turbulent regimes respectively.

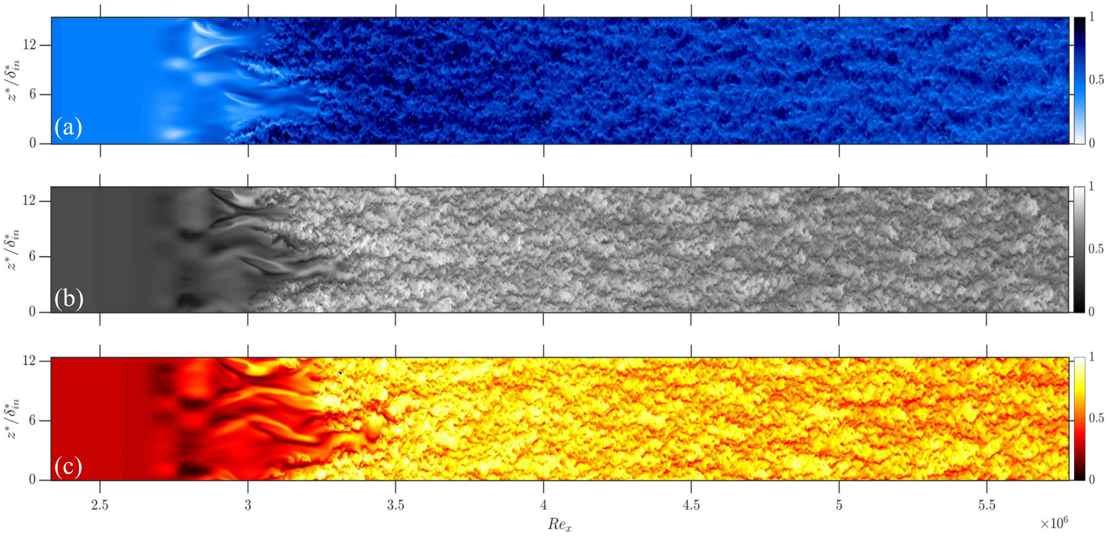

Figure 3: Instantaneous flow fields for (a) cooled, (b) adiabatic and (c) heated walls: contours of u^*/u^*_∞, shown at $y^*/\delta^*_{in} = 0.29$.

3. State of the turbulent boundary layer

Figure 2 represents the evolution of the compressible and the incompressible skin-friction coefficients C_f and $C_{f,inc}$ (averaged in time and the spanwise direction) in the domain for all the cases under consideration. In this study, we would regard the maximum value of C_f to mark the beginning of the fully developed turbulent region. C_f can be defined as:

$$C_f = \frac{\tau^*_w}{\frac{1}{2}\rho^*_\infty u^{*2}_\infty} \tag{15}$$

where, τ^*_w is the shear stress at the wall.

It can be seen from figure 2a that the boundary layer begins the transition to turbulence towards the end of the blowing/suction strip because of the high intensity of perturbation, which sets-in the by-pass transition scenario and no secondary instability region (usually marked by the formation of the streaks) is formed. The effect of disturbance is visible in the plot due to the high intensity of perturbation. Moreover, the levels of skin-friction coefficients rise consistently with decreasing wall-temperature in the transitional and the turbulent parts of the domain, because of the increasing local density close to the wall. More details regarding the effects of various physical parameters on the onset of transition can be found in [38, 39]. However, a contrasting trend is observed in case of the incompressible $C_{f,inc}$ (see figure 2b). These trends agree well with the findings reported by Shadloo et al. [27], Shadloo and Hadjadj [28]. Emperically, the compressible skin-friction coefficient for the laminar regime (marked by ····· in figure 2a) is given by [36]:

$$C_{f,lam} = 0.664 \times \frac{\sqrt{\rho^*_w \mu^*_w / \rho^*_\infty \mu^*_\infty}}{\sqrt{Re_x}} \tag{16}$$

while the analytical relation for the incompressible skin-friction coefficient for the fully developed turbulent region can be given as [27]:

$$C_{f,inc(turb)} = 0.074 \times \sqrt{\frac{\rho^*_{aw}}{\rho^*_w}} \times Re_x^{-0.2} \tag{17}$$

Hence, it can be seen in figure 2a that the fully developed turbulent region starts from $Re_x = 3.42 \times 10^6$, $Re_x = 3.46 \times 10^6$ and $Re_x = 3.57 \times 10^6$ for cooled, adiabatic and heated walls, respectively. Figure 3 displays the instantaneous flow visualizations of different cases showing the existence of the turbulent region in the majority of the domain.

Frequency spectra for the adiabatic case in the middle of the domain i.e. at $z^*/\delta^*_{in} = 7$ and $y^+ = 90$ at different streamwise locations; $Re_x = 3.02 \times 10^6$, 3.94×10^6 and 5.40×10^6 along with the -5/3rd slope of turbulence decay are plotted in figure 4a-c. It can be clearly seen in these spectra plots that as we

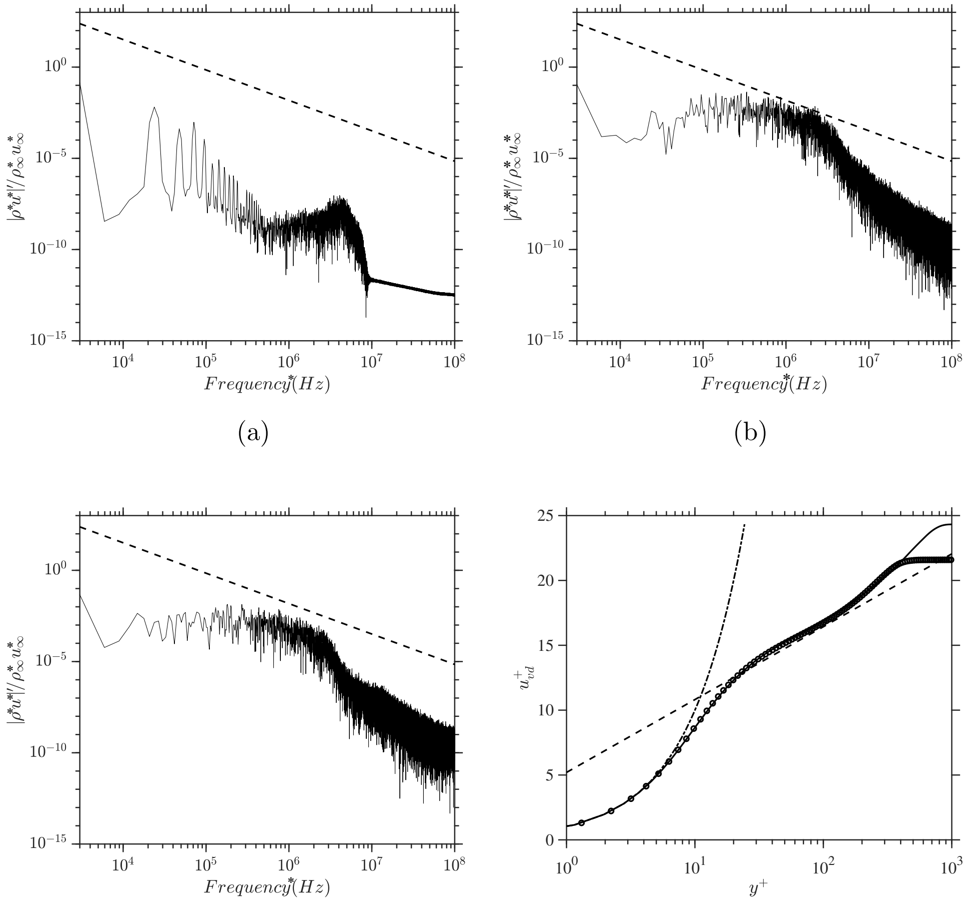

(a)

(b)

(c)

(d)

Figure 4: Frequency spectra of $|\rho^* u^*|'/\rho^*_\infty u^*_\infty$ for the adiabatic wall at (a) $Re_x = 3.02\times10^6$, (b) $Re_x = 3.94 \times 10^6$, (c) $Re_x = 5.40 \times 10^6$; where (- - -) represents the (-5/3) law of turbulence decay, and (d) Van-Driest transformed mean velocity profile for the adiabatic case compared with [23] (symbols) at $Re_x = 5.40\times10^6$, where (- - -) is ($1/0.41\ log\ y^+ + 5.2$) and (—··) is $u^+_{vd} = y^+$.

move from the transition region to the fully developed turbulent regime, the excitation frequency (23.87 kHz) does no longer remain prominently visible in the frequency spectrum. Therefore, it can be stated that the resulting turbulent statistics are not affected by the forcing frequency of the blowing and suction strip. Figure 4d shows the comparison of the Van-Driest transformed velocity profiles at $Re_x = 5.40 \times 10^6$ for the adiabatic case vs. Shadloo et al. [23] revealing the existence of fully developed turbulent flow because the viscous sublayer and the logarithmic regions are distinctly visible.

4. Joint probability density function and covariance integrands analyses

In this section, we will extensively employ the JPDF distribution and the covariance integrand analyses for investigating different properties affecting the flow topology of the supersonic turbulent boundary layers. These analyses would be used to describe various structural and dynamical aspects of the vortical structures and also to get a deeper insight about the physical mechanisms contributing the most to the turbulent shear-stress and the turbulent heat-flux. Both the JPDFs and the covariance integrands are plotted using the same bin size. It is to be noted that the results are reported for a fixed streamwise location in the fully turbulent part of the domain i.e. at $Re_x = 5.40 \times 10^6$. A grayscale color palette is used to represent the levels of the contours ranging from white (the minimum value) to black (the maximum value).

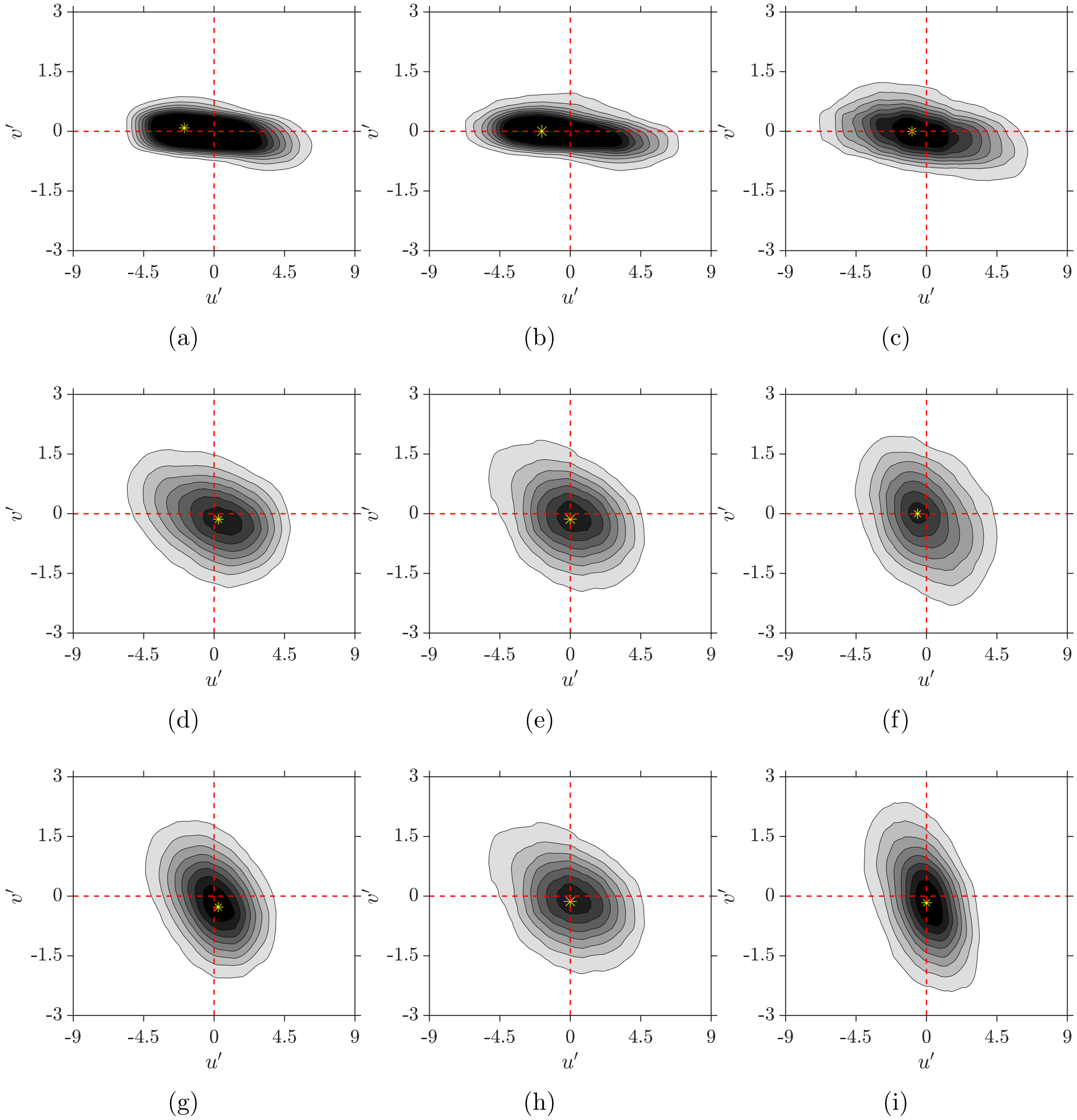

(a) (b) (c)

(d) (e) (f)

(g) (h) (i)

Figure 5: Contours of the joint probability density function (JPDF) distribution of the u' and v' at $y^+ = 10$ ((a)-(c)), 35 ((d)-(f)) and 90 ((g)-(i)). The colors of the contour levels vary from 1 to 8 (light to dark). Here the first, second and third columns represent the cooled, adiabatic and heated walls, respectively.

Table 2: Locations of the peaks for different cases shown in figure 5. The coordinates are marked as the (u', v') tuple.

y^+	C	A	H
10	(-1.906, 0.086)	(-1.815, 0.000)	(-0.926, 0.000)
35	(0.280, -0.139)	(0.000, -0.135)	(-0.571, 0.000)
90	(0.264, -0.276)	(0.000, -0.142)	(0.000, -0.166)

4.1. Velocity fluctuations

Figure 5 depicts the contour plots of the JPDF distribution of the fluctuations of the streamwise (u'^*) and wall-normal (v'^*) velocity components scaled by the local friction velocity $u^*_\tau = \sqrt{\tau^*_w/\rho^*_w}$ at various y^+ locations. In this figure, $u' = u'^*/u^*_\tau$ and $v' = v'^*/u^*_\tau$. Table 2 enlists the peak locations for the cases mentioned in the figure 5 (marked by the yellow *). The JPDF contours point out that the distribution of the v' is confined to a very small area in the buffer layer i.e. $y^+ = 10$, hence, the distribution is quite flat (figures 5a-c). A comparison of the figures 5a-c shows that, for the near-wall region, the peak tends to move towards zero (see first row of table 2) with increasing wall-temperature confirming the presence of the accelerated flow due to the increase in the momentum transfer process. Moreover, the peak locations marked in the first row of table 2 show negligible effects of the wall-temperature on the v' which is due to the strong viscous forces close to the wall. Similar behavior has been reported by Wallace and Brodkey [9] in case of the incompressible turbulent boundary layer. The comparison of the first and the second rows of the figure 5, reveals that on moving from the buffer layer to the log-region i.e $y^+ = 10$ to 35, the peak moves in the direction of the fourth quadrant which means that an increasing amount of fast moving flow going towards the wall (more details on the quadrant analysis will follow subsequently). However in the log-region, at $y^+ = 90$ (figures 5g-i), the positions of the peaks do not show a prominent variation (also see the third row of table 2) with respect to the wall-temperature. This means that the effects of the wall-temperature are confined to the near-wall region only. On comparing figures 5d to 5f with figures 5g to 5i, it can be observed that the distribution of v' grows more rapidly and dramatically with increase in y^+ as the wall temperature increases. This trend of growth mechanism shows an increased amount of wall-normal fluctuations in the log region with increasing wall-temperature, which generates higher levels of the turbulent shear-stress in the heated case. It should be noted here that the JPDF distribution tends to align its major axis with the corresponding dominant quadrants. From our discussion of this set of figures, it can be said that impact of wall heat transfer on the distribution of u' and v' can be seen predominantly in the buffer layer region.

In order to have a better insight about the flow topology, we would now use the quadrant analysis previously reported in [8, 9, 10]. The quadrant analysis of the contour plots of the covariance integrands provides a better understanding of various physical phenomena related to the corresponding quantities. Each quadrant represents a particular transfer process and the dominant quadrant represents the most influential of these. The turbulent shear-stress covariance, $\overline{u'v'}$ can be written as

$$\overline{u'v'} = \int \int_{-\infty}^{\infty} u'v'P(u',v')du'dv', \tag{18}$$

where, $P(u',v')$ is the joint probability density function of the u' and v' over

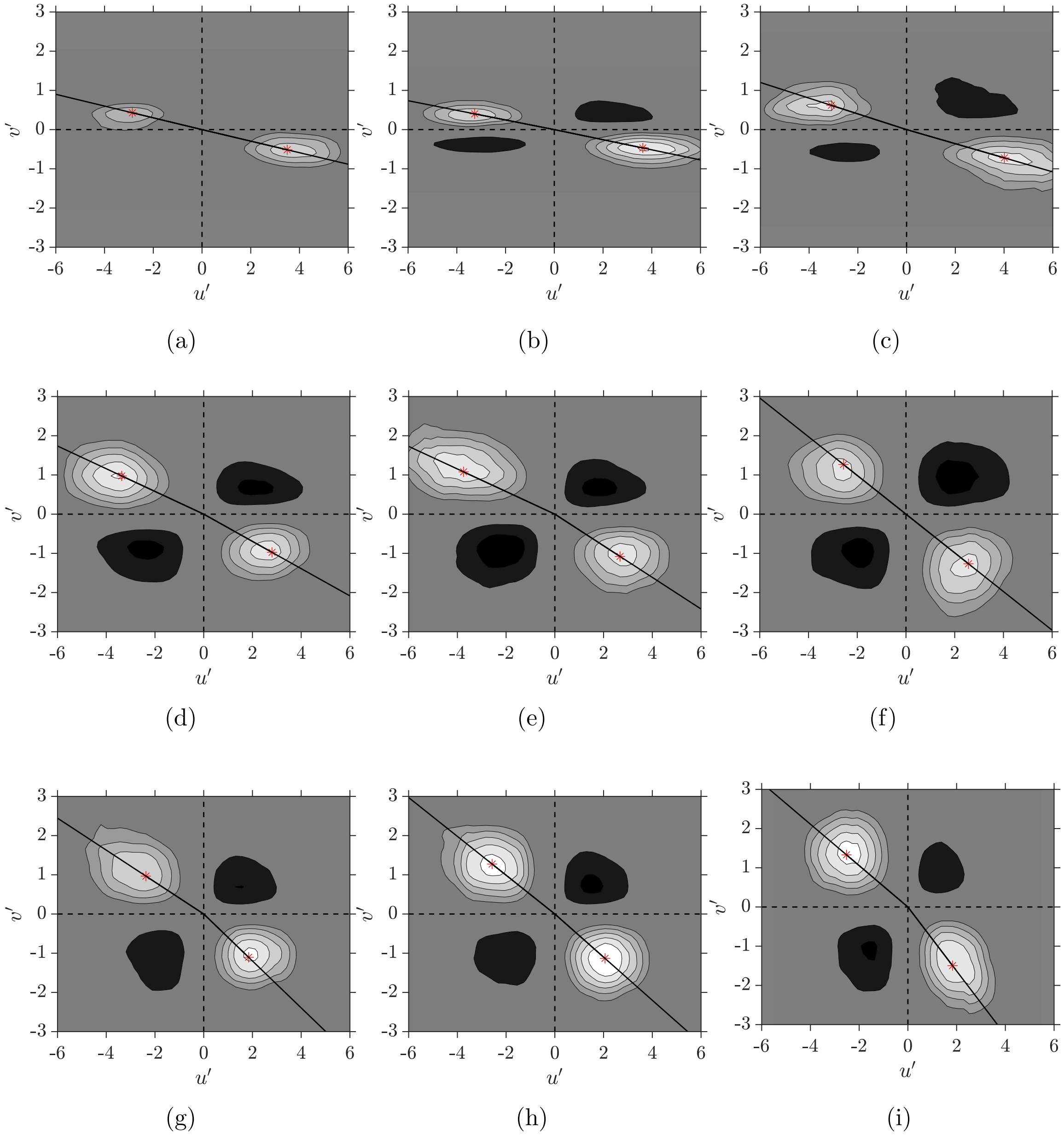

(a) (b) (c)

(d) (e) (f)

(g) (h) (i)

Figure 6: Contours of the covariance integrands of the u' and v' at $y^+ = 10$ ((a)-(c)), 35 ((d)-(f)) and 90 ((g)-(i)). The colors of the contour levels vary from -8 to 2, excluding the zero level (light to dark). Here the first, second and third columns represent the cooled, adiabatic and heated walls, respectively.

a bin area of $du'dv'$ and the quantity $u'v'P(u'v')$ is known as the covariance integrand.

The contour plots of the covariance integrands of $u'v'$ represent the contribution of signs and magnitude of a given component of velocity i.e. u' or v' towards the turbulent shear-stress covariance, $\overline{u'v'}$. The first quadrant (Q_1), where $u' > 0$ and $v' > 0$, represents the outward interactions. The second quadrant (Q_2), where $u' < 0$ and $v' > 0$, represents the events of ejections. The third quadrant (Q_3), where $u' < 0$ and $v' < 0$, represents the inward interactions, and the fourth one (Q_4), with $u' > 0$ and $v' < 0$, represents the sweeps [9, 10, 18].

Figure 6 represents the contour plots of the covariance integrands of the u' and v' for the corresponding y^+ positions mentioned in figure 5. In this figure, dark contours signify the positive contour levels i.e. levels 1 and 2 while the light ones are the negative contour levels (levels -8 to -1, see figure 5). The solid black lines in each plot serve as a visual reference for determining the angles of inclination with respect to the positive u' axis. These lines originate from the origin and pass through the peaks of the most dominant quadrants (marked by the red *). The changes in the angles of inclination quantify the shift in the observed physical phenomenon for the corresponding quadrant. At a glance of figure 6, it can be said that for all of the cases Q_2 and Q_4 are the dominant quadrants which means that the ejection and sweep mechanisms contribute the most to the turbulent shear stress. For incompressible channel flows, as per the findings of Wallace et al. [8], the ejections and sweeps contribute more than 100% towards the shear-stress, and additional stress generated is countered by the positive and negative interactions represented by the events of Q_1 and Q_3 respectively. Hence, the results shown in figure 6 are in good agreement with their incompressible counterparts. A closer look to this figure reveals that in the buffer region, at $y^+ = 10$, the sweeps are more important in comparison to the ejections in case of the cooled and to some extent for the adiabatic wall (figures 6a and b) because there exists an additional lower contour level. This means that the high-speed fluid moving towards the wall is the major contributor to the turbulent shear-stress. However, figure 6c suggests that for $y^+ = 10$, the ejections and sweeps become comparable for the heated wall. Therefore, it can be said that in the buffer-region, decrease in wall-temperature favors the sweep events. At $y^+ = 35$ (figures 6d-f), it can be seen that the ejection events are dominant for the cooled and the adiabatic walls, whereas for the heated wall, both the ejections and sweeps become comparable, which means that the decreasing wall-temperature favors the ejections. Towards the end of the log-region, at $y^+ = 90$, the ejections and the sweeps are comparable for the cases A and H while for the case C sweeps contribute the most towards the shear-stress covariance.

4.2. Vorticity fluctuations

In this section we would talk about the topology and the physical orientation of the coherent structures in the flow field. The JPDF and the covariance integrand contours of the vorticity components shed some light on the flow topology. The alignment of these contours indicates the most-likely orientation of the projections of the coherent structures at that given position in different planes. It should be noted here that this representation is global in nature and reveals the most-likely inclinations of the projections

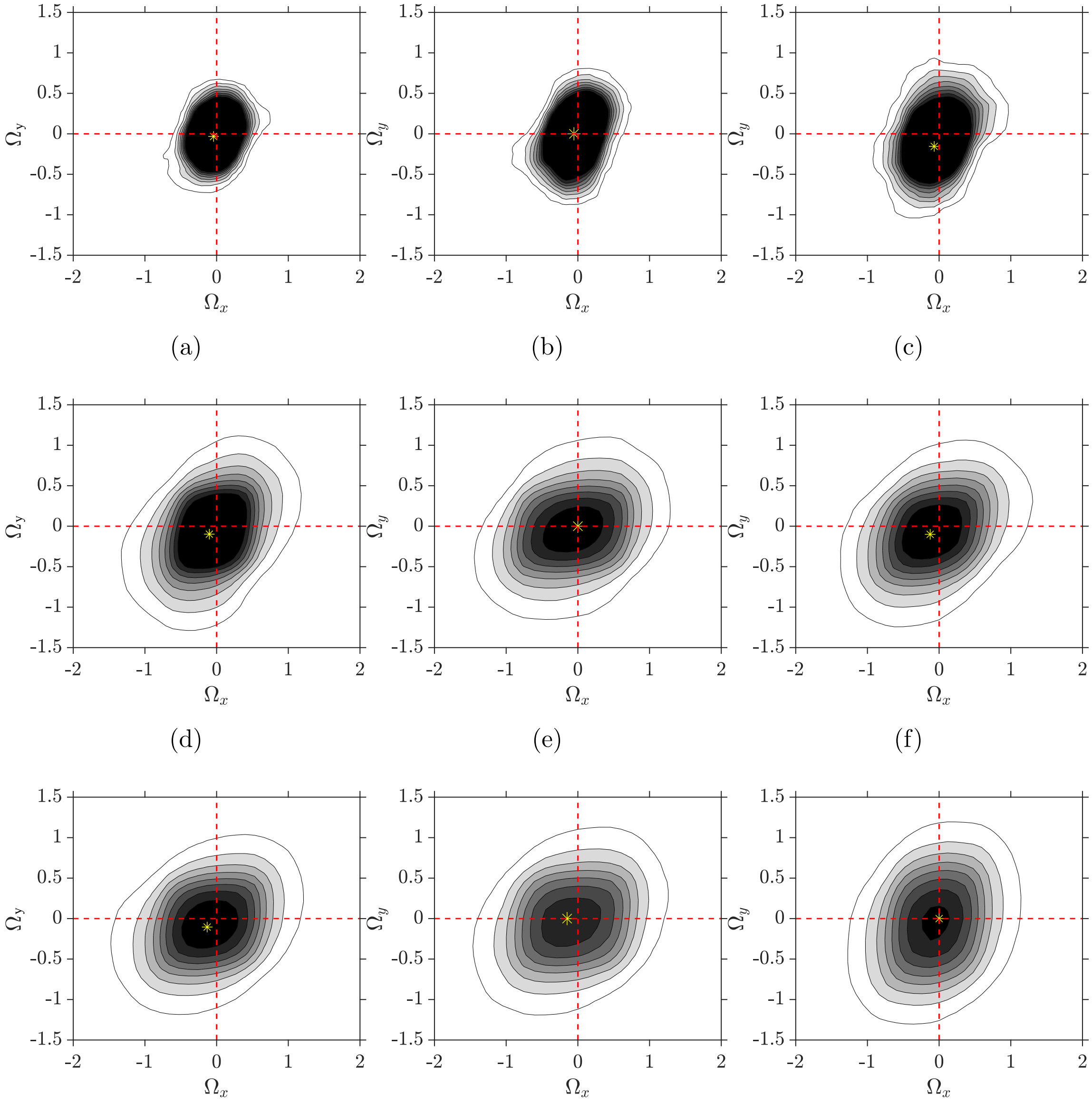

(a) (b) (c)

(d) (e) (f)

(g) (h) (i)

Figure 7: Contours of the JPDF distribution of the Ω_x and Ω_y at $y^+ = 10$ ((a)-(c)), 35 ((d)-(f)) and 90 ((g)-(i)). The colors of the contour levels vary from 5 to 40 (light to dark). Here, the first, second and third columns represent the cooled, adiabatic and heated walls, respectively.

of the coherent structures in three-dimensional sense. The structures present in the turbulent field can have any sense of rotation or they may exist in pairs of counter-rotating vortices which in three-dimensional sense represent a hairpin (or lambda) structure. Other possibilities of flow configuration also exist such as the hairpin forests [6], or the cane structures (or asymmetrical hairpins) [18] among others.

Figure 7 displays the contours of the JPDF distribution of the streamwise and wall-normal vorticity components; Ω_x^* and Ω_y^* respectively which are normalized by the local vorticity magnitude i.e. $\Omega_x = \Omega_x^*/\Omega^*$ and $\Omega_y = \Omega_y^*/\Omega^*$, where $(\langle\Omega^*\rangle = \sqrt{\Omega_x^{*2} + \Omega_y^{*2} + \Omega_z^{*2}})$, $\langle\rangle$ represents local time-averaged quantity, and $\Omega_x^* = \frac{\partial w^*}{\partial y^*} - \frac{\partial v^*}{\partial z^*}$, $\Omega_y^* = \frac{\partial u^*}{\partial z^*} - \frac{\partial w^*}{\partial x^*}$ and $\Omega_z^* = \frac{\partial v^*}{\partial x^*} - \frac{\partial u^*}{\partial y^*}$. These contours represent the most probable projections of the coherent structures in the streamwise-wall-normal plane (x-y plane) at some angle to the wall that can vary along the length of the vortical structure [11]. The orientation of these contours shows the positive correlation between the two quantities which is obvious due to the high-speed of the flow in the streamwise direction. On comparing the first, second and third rows of figure 7 it can be stated that the contours' orientation increases in the streamwise direction which is due to the increment in the streamwise velocity with increasing y^+. Moreover, it can be seen from these figures that the wall-temperature does not has significant impact on the inclination of the contours.

The contours of the covariance integrands of Ω_x and Ω_y i.e. $\Omega_x\Omega_y P(\Omega_x, \Omega_y)$ are shown in figure 8. It should be noted that, for this quadrant analysis, the physical significance of each quadrant is not the same as stated before for figure 6. In this case, the dominant quadrants highlight the most-likely

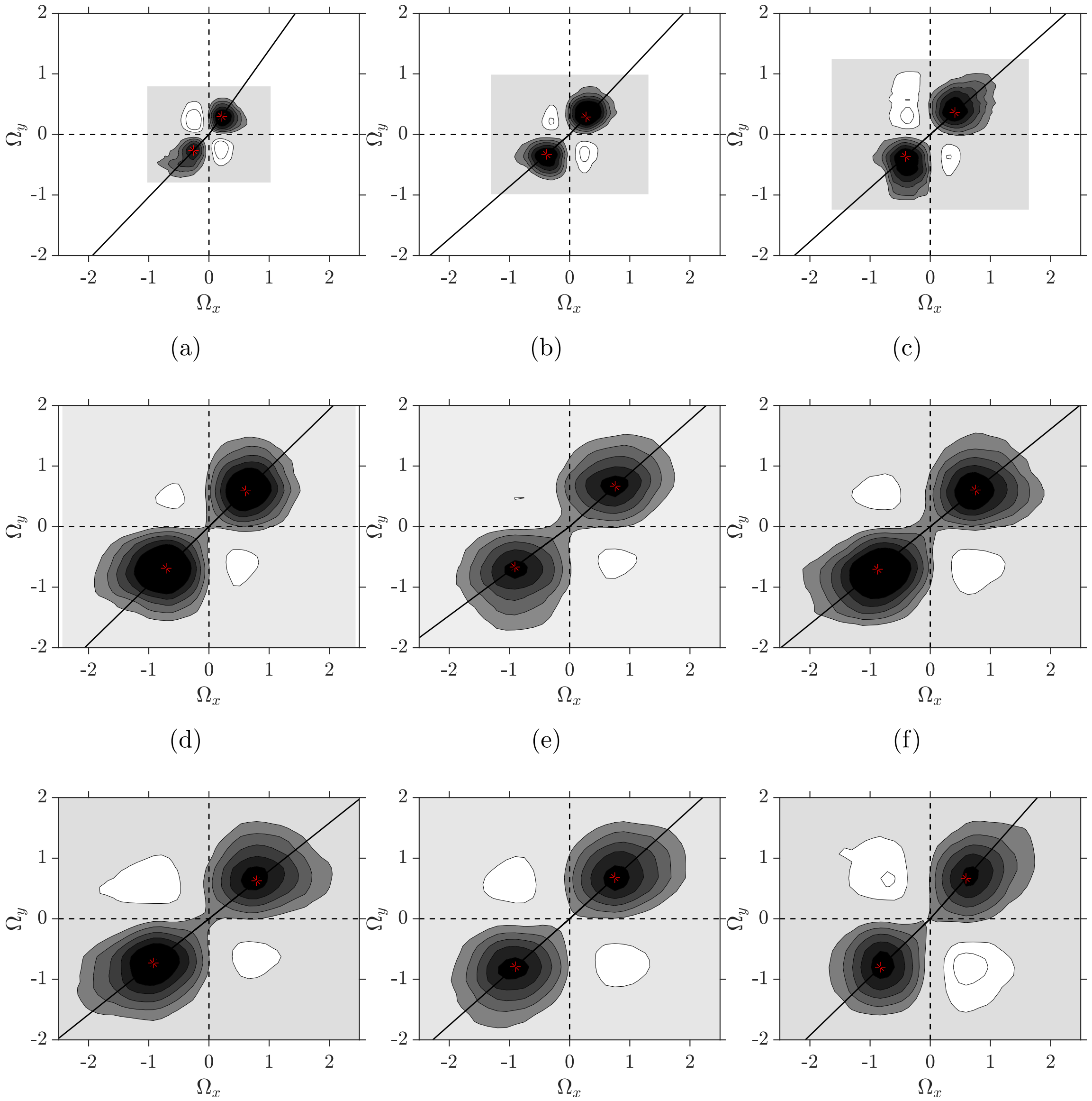

(a) (b) (c)

(d) (e) (f)

(g) (h) (i)

Figure 8: Contours of the covariance integrands of the Ω_x and Ω_y at $y^+ = 10$ ((a)-(c)), 35 ((d)-(f)) and 90 ((g)-(i)). The colors of the contour levels vary from -0.5 to 3, excluding the zero level (light to dark). Here the first, second and third columns represent the cooled, adiabatic and heated walls, respectively.

orientation of the vorticity filaments (their projections) at the given locations which contribute to the covariance $\overline{\Omega_x \Omega_y}$. It can be clearly seen from these plots that as a result of the positive correlation between the two quantities, Q_1 and Q_3 are the dominant quadrants here. The orientation of the projections of the vorticity filaments in the (x-y) plane can be given as

$$\alpha = \tan^{-1}\left(\frac{\Omega_y}{\Omega_x}\right) \tag{19}$$

α is the angle made by the peaks of the dominant quadrants (Q_1 and Q_3 here) with respect to the positive Ω_x-axis. The solid black lines are marked to serve as a visual aid to estimate the angles of inclination. In figures 8a-c, the white regions surrounding the gray rectangles are the areas with no data. On comparing the inclinations of the vorticity filaments at different y^+ positions, it can be observed that α is 54°, 44° and 38° in Q_1 and -134°, -136° and -142° in Q_3 for $y^+ = 10$, 35 and 90, respectively for the cooled wall (i.e. figures 8a, d and g). This trend suggests that on moving from the buffer layer ($y^+ = 10$) to the log region ($y^+ = 35$), the filaments tend to rotate in the streamwise direction. The same trend is observed for all the three cases when moving from $y^+ = 10$ to 35 (see first two rows of table 4). However, for the adiabatic wall, the α is about 46°, 41° and 42° in Q_1 and -139°, -144° and -139° in Q_3 respectively. Hence, the adiabatic wall shows subtle variation in the log-region (angles in Q_1), this trend is similar to the one reported by Ong and Wallace [11] for the incompressible turbulent flows (keeping in mind the ±5° error for the bin size used by them). The visual inspection of the orientation and dominance of the quadrants with the literature reveals that the results of both the cooled as well as the adiabatic walls bear close similarities with the results of the compressible flows [26] (due to the different

Table 3: Locations of the peaks for different cases shown in figure 9. The coordinates are marked as the (Ω_x, Ω_z) tuple.

y^+	C	A	H
10	(0.000, -0.983)	(0.000, -0.884)	(-0.068, -0.889)
35	(-0.102, -0.497)	(0.000, -0.398)	(-0.125, -0.456)
90	(-0.132, -0.304)	(-0.150, -0.286)	(-0.119, -0.348)

y^+ locations reported, a direct comparison is not possible). However, for the heated wall, the inclination angles decrease in the early log region followed by a strong increase i.e. 42°, 39° and 48° in Q_1 for $y^+ = 10$, 35 and 90, respectively. This variation in the trend of inclination means that in the log region the wall-normal vorticity component is still on the rise due to increased heat-transfer from the wall. A comparison between the angles of inclination of the second and the third rows of figure 8 (see table 4) reveals that on moving from $y^+ = 35$ to 90, the vortical filaments tend to orient themselves lesser in the streamwise direction (as evident from the increasing values of α) with increasing wall-temperature. Therefore, from our discussion of about this set of figures, it can be stated that the wall temperature affects the usual orientation of the vorticity filaments in the buffer-layer region as well as in the log-region due to the strong heat transfer.

Now, we consider the orientation of the projections of the coherent structures in the x-z plane (streamwise-spanwise plane). Figure 9 shows the JPDF distribution, $P(\Omega_x, \Omega_z)$ of the streamwise and the wall-normal vorticity components, Ω_x^* and Ω_z^*, respectively which are normalized by the time-averaged local vorticity magnitude $\langle \Omega^* \rangle$ at different y^+ positions for all the three cases

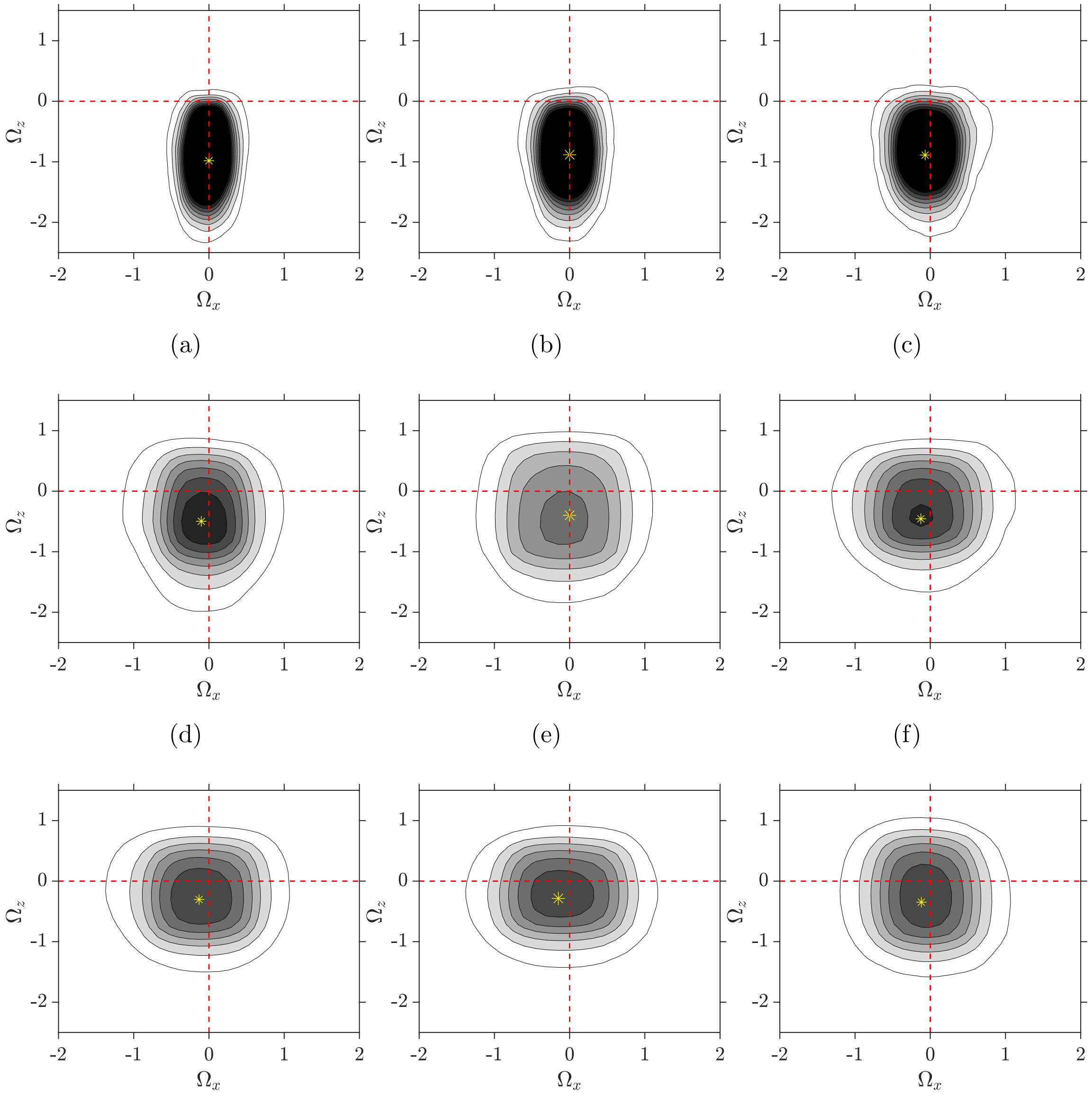

(a) (b) (c)

(d) (e) (f)

(g) (h) (i)

Figure 9: Contours of the JPDF distribution of the Ω_x and Ω_z at $y^+ = 10$ ((a)-(c)), 35 ((d)-(f)) and 90 ((g)-(i)). The color of the contour levels vary from 5 to 40 (light to dark). Here the first, second and third columns represent the cooled, adiabatic and heated walls, respectively.

(A, C and H), and table 3 enlists the peak locations for the same cases. It can be seen in these figures that in the buffer layer, $y^+ = 10$ (figures 9a to 9c) the JPDF contours are somewhat triangular in shape. This triangular shape becomes predominant with increasing wall-temperature which indicates a net increase in the magnitude of Ω_x as the wall-temperature rises. As we progress farther from the buffer-layer region ($y^+ = 10$) to the log-region ($y^+ = 35$), the contours start to get more dilated in the Ω_x direction irrespective of the wall-temperature, however, the peak remains in the vicinity of zero for the Ω_x-axis (see table 3). The dilatation of the contours gets increased with increasing wall-temperature (figures 9a to f) which means that increasing wall-temperature also increases the net magnitude of Ω_x. These triangular shapes of JPDF contours imply that the vorticity filaments do not show much inclination in the streamwise direction and the spanwise vorticity component (Ω_z) largely remains negative, meaning that it has the same sign as that of the mean shear. It can be clearly seen from table 3 that there exists a considerable shift in the location of the peak towards the positive Ω_z-axis ($\approx 50\%$) irrespective of the wall-temperature as one moves to the higher y^+ locations which implies a sudden and dramatic increase of the wall-normal vorticity component. This comparison of the peak location also reveals that the shift of the peak locations is less significant with increasing wall-temperature. From figure 9, it can be concluded that Ω_z is dominant in comparison to Ω_x because the location of the peak never changed considerably in the Ω_x-axis.

Figure 10 shows the plots of the contours of the covariance integrand of the Ω_x and Ω_z at different y^+ locations. The white regions around the dark

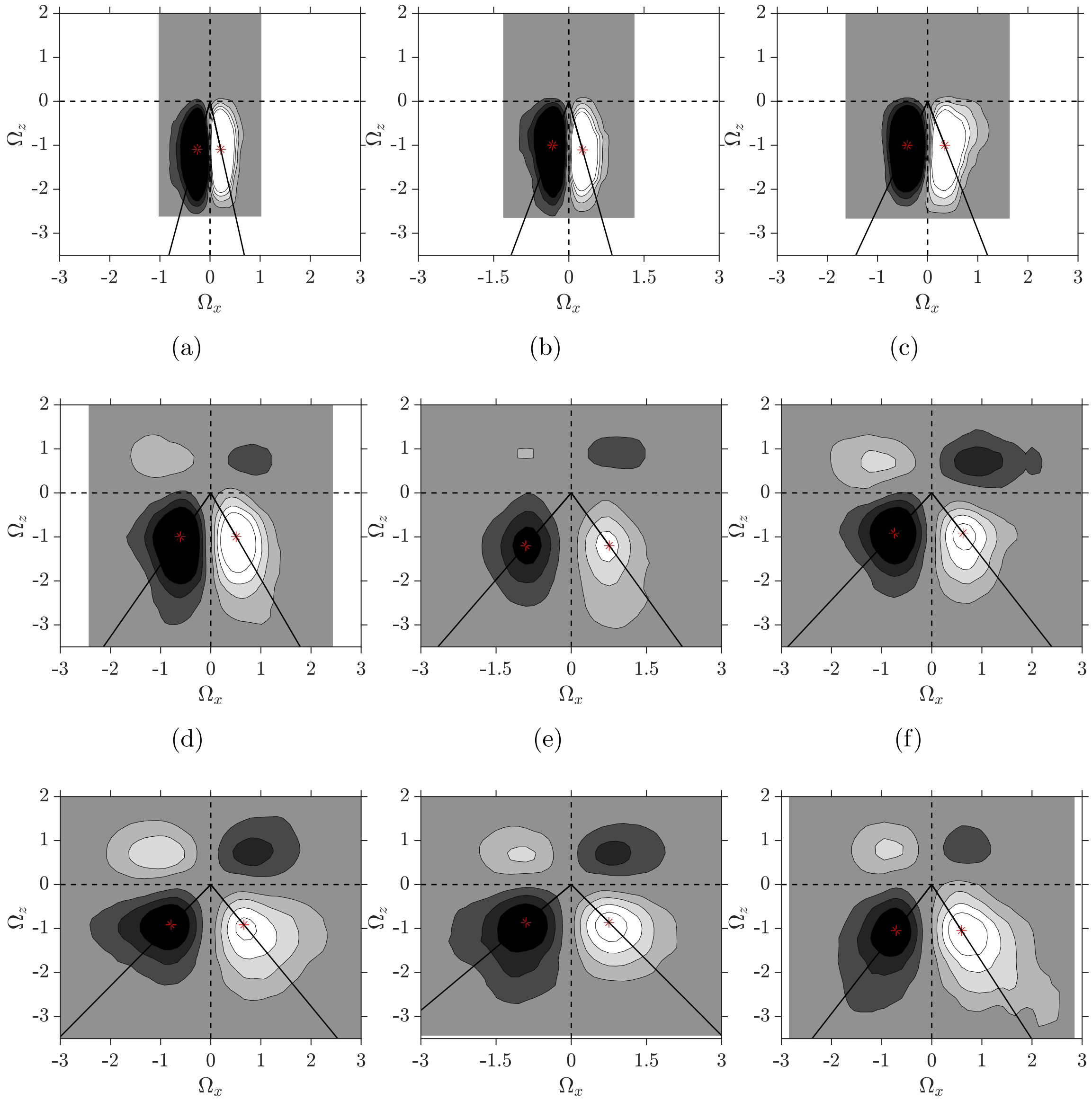

(a) (b) (c)

(d) (e) (f)

(g) (h) (i)

Figure 10: Contours of the covariance integrands of the Ω_x and Ω_z at $y^+ = 10$ ((a)-(c)), 35 ((d)-(f)) and 90 ((g)-(i)). The color of the contour levels vary from -2 to 1.5, excluding the zero level (light to dark). Here the first, second and third columns represent the cooled, adiabatic and heated walls, respectively.

rectangles in figures 10a-d and i are the regions without any data. In the buffer-layer ($y^+ = 10$, figures 10a-c), no contour levels exist in the Q_1 nor in the Q_2 which is consistent with figures 9a-c which show that the JPDF distribution of Ω_x and Ω_z exists only in the Q_3 and Q_4. Therefore, figure 10 clearly shows that the Q_3 and Q_4 are the dominant quadrants. The angles of inclination of projections of the vorticity filaments in the x-z plane (represented by the solid black lines) can be defined as

$$\beta = \tan^{-1}\left(\frac{\Omega_x}{\Omega_z}\right). \tag{20}$$

These inclinations are mentioned here with respect to the negative Ω_z-axis. Like before, the counter-clockwise sense is considered as the positive sense of rotation while the clockwise sense is the negative one. On moving from the buffer-layer to the log-region; from $y^+ = 10$ to 35, the inclination angles increase for all the cases (see table 4). Moreover, for these locations, the angles of inclination increase with increasing wall-temperature. For case C, in the buffer layer region, i.e. $y^+ = 10$ (figure 10a), the vortical filament projections are inclined at 11° and -13° in the Q_4 and Q_3 quadrants, respectively. These low values imply that in the x-z plane, the coherent structures are primarily oriented in the negative spanwise direction. However, with an increment in the distance from the wall, the filaments tend to rotate in the streamwise direction resulting in the augmentation of the angles of inclination to 27° and -31° for the Q_4 and Q_3, respectively at $y^+ = 35$, and to 36° and -41° at $y^+ = 90$. The same trend is observed for the adiabatic wall as well (see table 4). Significant differences exist regarding the angles of inclination for the heated wall at different y^+ locations because of the increased transfer processes due to higher wall-temperature. Notably, at $y^+ = 90$, the values

Table 4: Angles of inclination of the projections of the vorticity filaments for different cases at various y^+ positions.

	Cooled wall				Adiabatic wall				Heated wall			
	α		β		α		β		α		β	
y^+	Q_1	Q_3	Q_3	Q_4	Q_1	Q_3	Q_3	Q_4	Q_1	Q_3	Q_3	Q_4
10	54	-134	-13	11	46	-139	-18	14	42	-138	-22	19
35	44	-136	-31	27	41	-144	-37	32	39	-141	-39	34
90	38	-142	-41	36	42	-139	-40	35	48	-136	-34	30

of β decrease for the heated wall (see table 4). This can be explained by the JPDF distribution shown in figure 9i, which shows a dramatic increase in the distribution of the Ω_z as a consequence of the increased wall-temperature. Hence, the distribution of Ω_x slightly shrinks. Therefore, it can be said that the wall-temperature affects the topology of the vortical elements in the x-z plane also in both the buffer-layer and the log-region.

Table 4 enlists all the values of α and β for all the cases at different y^+ positions, and also brings out the impacts of wall temperature on these angles. From this table, it can be clearly interpreted that the wall-temperature affects the turbulent flow topology in both the buffer-layer as well as the log-region for the SBLs.

4.3. Streamwise velocity component and temperature fluctuations

So far, we have discussed the kinetic aspects of the flow in detail which dealt with the velocity fluctuations and the vorticity components. For this study, we are utilizing different wall temperatures, hence, it becomes vital to investigate the implications of the wall-temperature on the heat-flux. More-

Table 5: Locations of the peaks for different cases shown in figure 11. The coordinates are marked as the (u', T') tuple.

y^+	C	A	H
5	(-1.145, -0.004)	(-1.391, 0.013)	(-1.221, 0.011)
10	(-1.906, -0.000)	(-1.815, 0.026)	(-0.926, 0.026)
35	(0.280, -0.006)	(-0.268, 0.000)	(-0.570, 0.025)
90	(-0.264, -0.006)	(0.000, -0.009)	(0.000, -0.029)

over, in the supersonic regime, the wall-temperature is one of the important factors to be looked into because it is impacted by different physical quantities like the local density and viscosity which themselves are affected by the compressibility.

Figure 11 shows the JPDF distribution of the streamwise velocity fluctuations (u'^*) and the temperature fluctuations (T'^*) for all the cases at different y^+ locations, and table 5 enlists the locations of the peaks for the corresponding cases. In this figure, an additional location in the viscous sub-layer ($y^+ = 5$) is also shown, in order to explore the near-wall region in greater detail. Here, the temperature axis is scaled by the time-averaged local temperature, $\langle T^* \rangle$ and the velocity by the local friction velocity (u^*_τ). The relation between the u' and the T' represents the turbulent heat-flux in the streamwise direction. For the rest of the manuscript, the correlation and the anti-correlation between the mentioned quantities refers to the existence of the positive, and the negative slopes respectively of the JPDF contours with the axis of abscissae. A comparison of the figures 11a to 11c highlights the effects of the wall-temperature in the viscous sub-layer. It can be

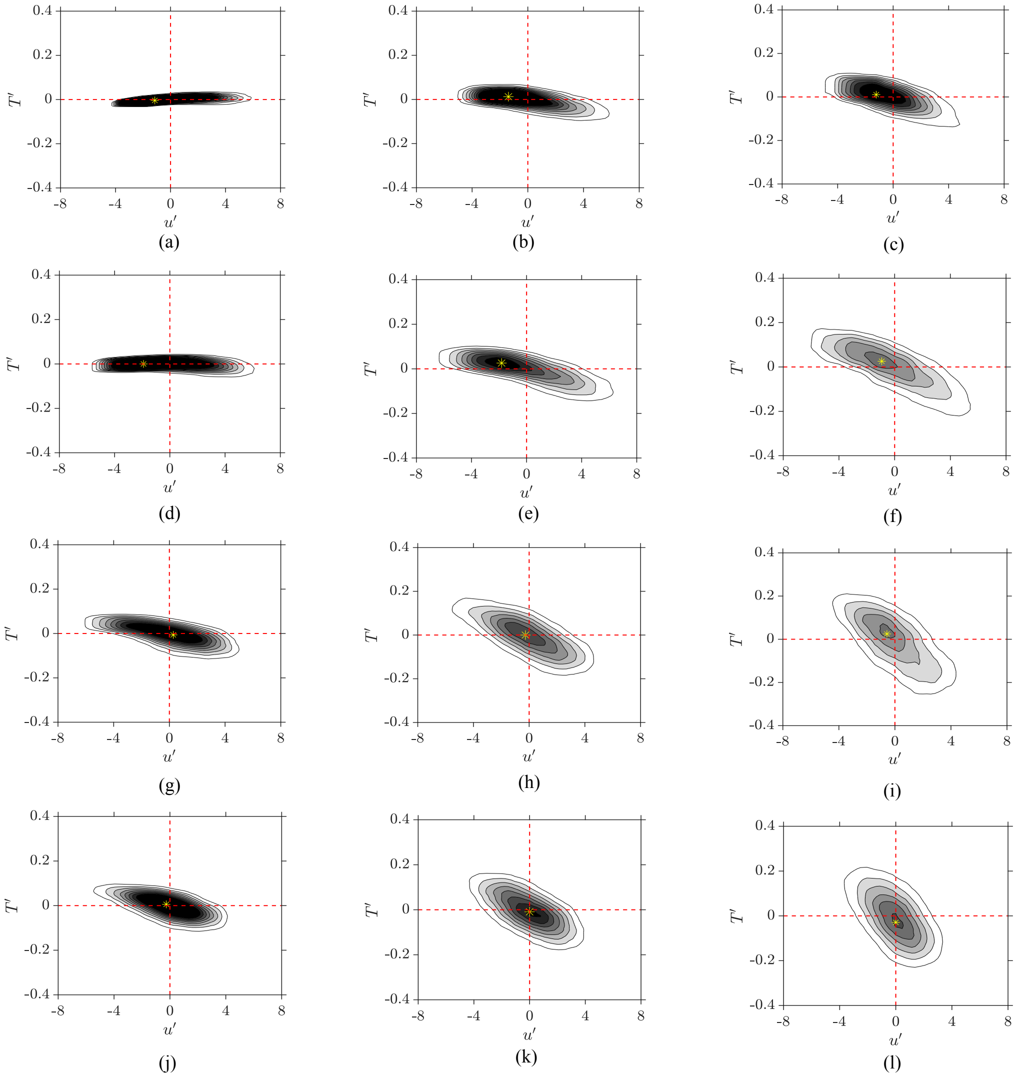

(a) (b) (c)

(d) (e) (f)

(g) (h) (i)

(j) (k) (l)

Figure 11: Contours of the JPDF distribution of the u' and T' at $y^+ = 5$ ((a)-(c)), 10 ((d)-(f)), 35 ((g)-(i)) and 90((j)-(k)). Here the first, second and third columns represent the cooled, adiabatic and heated walls, respectively. the color of the contour levels vary from 15 to 120 (light to dark).

seen that in case of the cooled wall, in the viscous sub-layer, the u' and T' are directly correlated, while a clear anti-correlation can be seen in case of the adiabatic and the heated walls. This trend has been reported by Duan et al. [2], Lechner et al. [22], Shadloo et al. [23] for the supersonic turbulent flat plates and the channel flows. This set of figures clearly reveals a trend of change in the orientation of the major axis of the JPDF contours with increment in the y^+ with respect to the u' axis. For case C, in the buffer layer region (at $y^+ = 10$), the JPDF contours become parallel to the u' axis representing a flat distribution. It can be seen from figure 11d that the peak of u' is shifted to the negative side (see first column of table 5) which implies the existence of the retarded flow in the streamwise direction. On the other hand, the flow is comparatively less retarded for the adiabatic and the heated walls. This clearly indicates that in the buffer-layer region $y^+ = 10$, the increasing wall-temperature tends to decrease the deceleration of the flow in the streamwise direction. For the higher y^+, the u' and the T' become anti-correlated for the cooled wall. However, the adiabatic and the heated cases remain anti-correlated from the viscous sub-layer itself. It can be clearly seen from the figures 11g-l that in the log-region, for all the cases, the peak location remains very close to zero (see table 5) which indicates the existence of the homogenous turbulence. This set of figures also clarifies that the increasing wall-temperature favors the anti-correlation between the u' and the T'.

The contours of the covariance integrands of the u' and T', i.e. $u'T'P(u', T')$ are shown in figure 12 which represent the contributions of the u' and the T' towards the streamwise component of the heat-flux, $\overline{u'T'}$. In order to

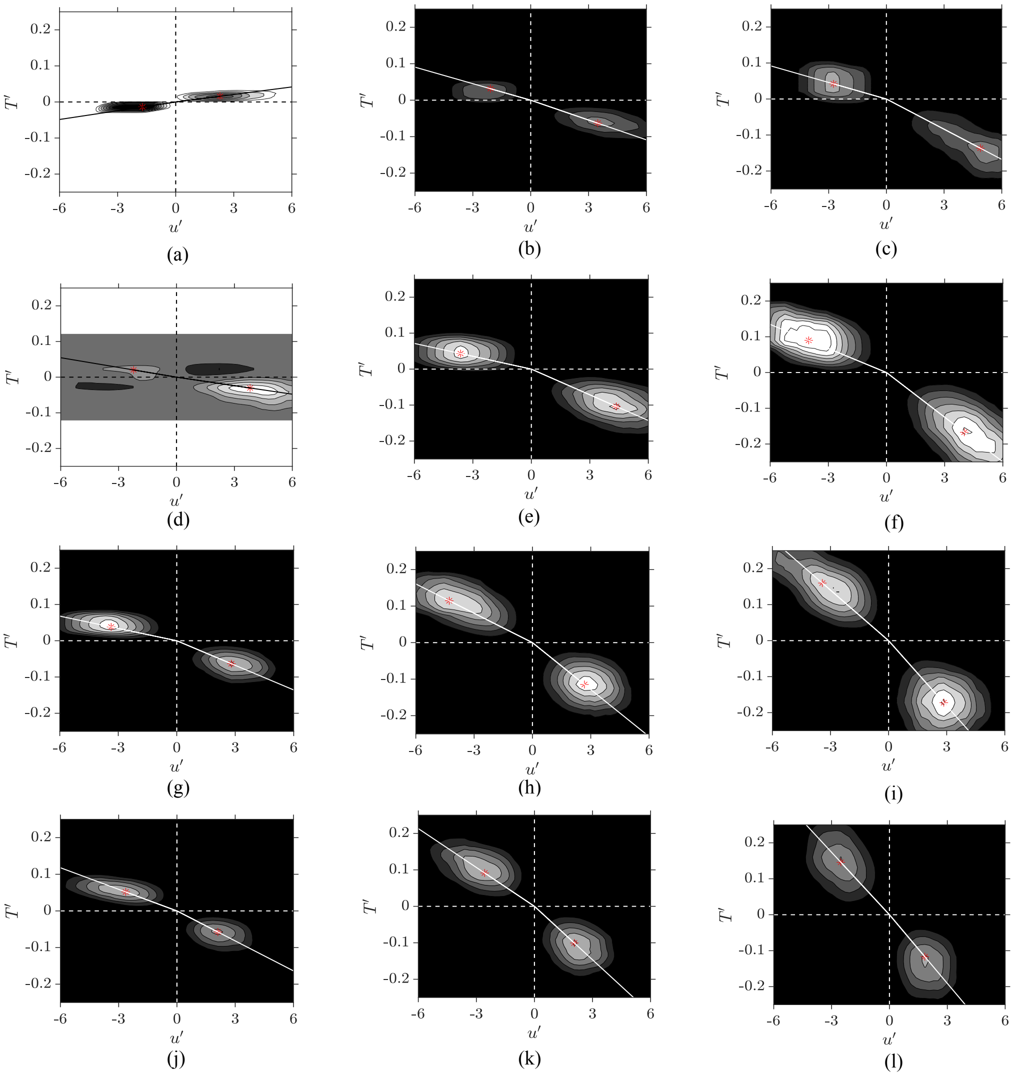

Figure 12: Contours of the covariance integrands of the u' and T' for $y^+ = 5$ ((a)-(c)), 10 ((d)-(f)), 35 ((g)-(i)) and 90((j)-(l)). Here the first, second and third columns represent the cooled, adiabatic and heated walls, respectively. The colors of the contour levels vary from 2 to 9 (light to dark) for (a), from -5 to 2, excluding the zero level for (d) and from -16 to -4 for the rest.

understand the physical phenomena responsible for this transfer process, we present the following quadrant analysis. The first quadrant (Q_1), where $u' > 0$ and $T' > 0$, indicates fast moving heated fluid. The second quadrant (Q_2), with $u' < 0$ and $T' > 0$, indicates slow moving heated fluid. The third quadrant (Q_3), having $u' < 0$ and $T' < 0$, means that the cooled fluid is moving slower while the fourth quadrant (Q_4), where $u' > 0$ and $T' < 0$, denotes the events of fast moving cooled fluid. As can be seen, in all the figures except figure 12a where clear dominance of the Q_1 and Q_3 can be seen, the Q_2 and Q_4 are the dominant quadrants owing to the anti-correlation between the u' and T'. For the cooled wall, at $y^+ = 5$ (figure 12a), Q_3 is dominant in comparison to Q_1 which means that the slow moving cold fluid contributes more to the turbulent heat-flux in the streamwise direction than the fast moving hot fluid. In the buffer-layer, at $y^+ = 10$ (figure 12d), where the change in the inclination of the contours is registered, it can be seen that Q_4 is more dominant in comparison to Q_2, highlighting the fact that fast moving cooled fluid has more contribution towards the streamwise turbulent wall heat-transfer. In case of the adiabatic and the heated walls, it can be seen that the major contribution comes from Q_2 than Q_4, extending from the viscous sub-layer to the log region. The comparable dominance of the Q_2 and Q_4 implies the existence of homogeneous turbulence towards the outer layer. It can also be observed from these figures that on moving away from the surface of the wall i.e. towards the higher y^+, the angles of inclination of the contours also increase because of the increased perturbations. From this comparison we can state that for the cooled wall, the effects of wall temperature on the streamwise turbulent heat-flux can be seen from the viscous sub-layer to the buffer-layer. And, in the log-region, the wall temperature does not has significant effects due to the turbulent mixing happening in the outer layers.

4.4. Wall-normal velocity component and temperature fluctuations

In order to have a complete overview of the heat-transfer phenomenon, we would now focus on the wall-normal component of the turbulent heat-flux which is given by the covariance of the wall-normal velocity and temperature fluctuations. The contours plots of the JPDF distribution of the wall-normal velocity fluctuations (v'^*) and temperature fluctuations (T'^*) are shown in figure 13. Here, the velocity and the temperature fluctuations are scaled by the local friction velocity (u^*_τ) and the time-averaged local temperature $\langle T^* \rangle$, respectively. Likewise in figure 11, a comparison between the figures 13a to 13c highlights a different trend in case of the cooled wall, as in the viscous sub-layer the quantities v' and T' are weakly anti-correlated while they exhibit a subtle correlation for the other two cases (A and H). For case C, on moving towards higher y^+, we see that at $y^+ = 10$, the major axis of the JPDF contours becomes parallel to the v' axis and the distribution becomes flat, and the peak of the contours remains close to the origin. However, in the log region, figures 13g and 13j, the major axis of the contours aligns itself in the Q_1 and Q_3 in an anti-clockwise sense which means that more amount of fluid is going towards the wall. This set of figures shows that for the adiabatic and the heated walls, the quantities v' and T' show correlation from the viscous sublayer itself. This means that the effects of temperature on the turbulent boundary layers can be seen from the viscous sublayer to the buffer-layer region. Afterwards, for $y^+ \geq 35$, as a result of the turbulent mixing, the

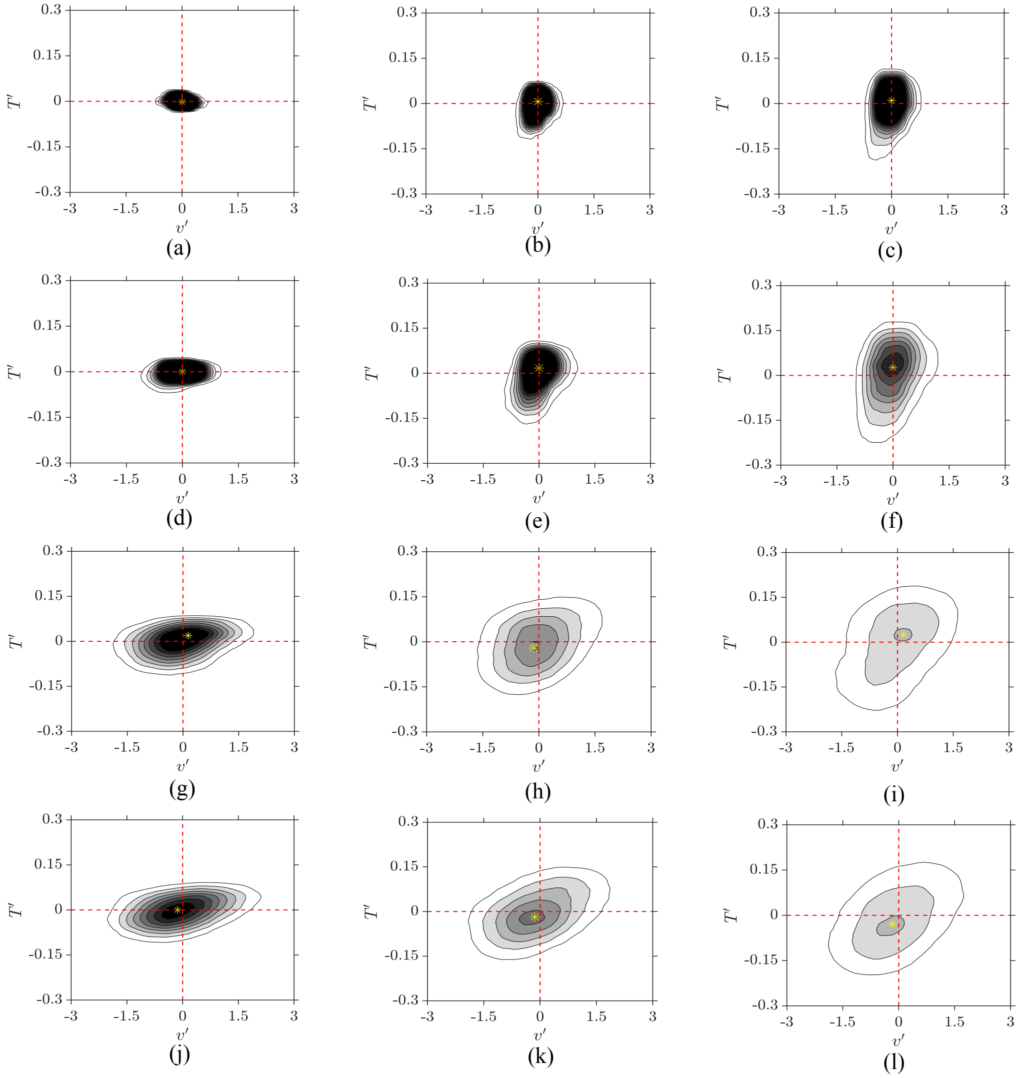

(a) (b) (c)

(d) (e) (f)

(g) (h) (i)

(j) (k) (l)

Figure 13: Contours of the JPDF distribution of the v' and T' for $y^+ = 5$ ((a)-(c)), 10 ((d)-(f)), 35 ((g)-(i)) and 90 ((j)-(l)). Here the first, second and third columns represent the cooled, adiabatic and heated walls, respectively. The color of the contour levels vary from 40 to 320 (light to dark).

differences arising from the wall-temperature are not so significant in terms of the peak position, but the maximum value of the JPDF contours does decrease with increasing wall-temperature.

We would now discuss about the contour plots of the covariance integrand of the v' and T' i.e. $v'T'P(v', T')$ in order to reveal the contributions of different physical phenomena towards the turbulent wall-normal heat-flux covariance, $\overline{v'T'}$. Following quadrant analysis is presented for the $v'T'$ plane. The first quadrant (Q_1), with $v' > 0$ and $T' > 0$, indicates that the heated fluid is moving away from the wall. The second quadrant (Q_2), where $v' < 0$ and $T' > 0$, means that the heated fluid moving down towards the wall. The third quadrant (Q_3), with $v' < 0$ and $T' < 0$, highlights the events where cooled fluid moves towards the wall while the fourth quadrant (Q_4), with $v' > 0$ and $T' < 0$, indicates the events of the cooled fluid moving away from the wall. The contours of the covariance integrands of the v' and T' are shown in figure 14 for all the cases at different y^+ locations. Like before, the white region surrounding the gray rectangles represents the region with no data. It should be noted here that in order to have a clear representation, figure 14a, and figures 14b and c are zoomed-in by four and two times respectively for both the axes with reference to the planes' dimensions used for figures 14d to l. It can be seen in figure 14 that for all the cases the Q_1 and Q_3 are the dominant quadrants except for figure 14a where the Q_2 and Q_4 are dominant. In the viscous sub-layer, at $y^+ = 5$, it can be seen that for the cooled wall, the Q_2 is more dominant in comparison to the Q_4 which means that the heated fluid is going towards the wall has more contribution towards the turbulent wall-normal heat-flux which is the reason why the wall is behaving as the

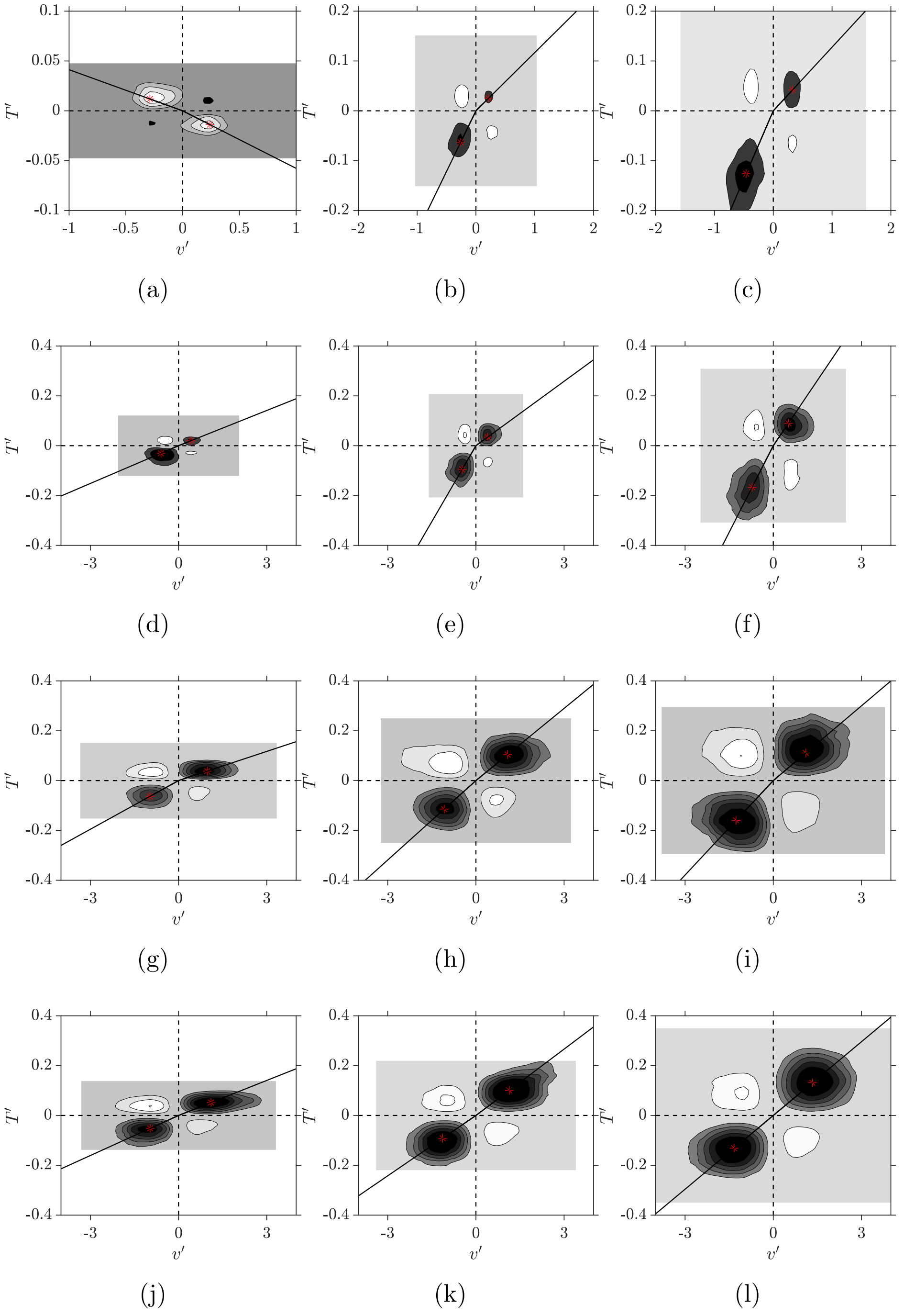

(a) (b) (c)

(d) (e) (f)

(g) (h) (i)

(j) (k) (l)

Figure 14: Contours of the covariance integrands of the v' and T' at $y^+ = 5$ ((a)-(c)), 10 ((d)-(f)), 35 ((g)-(i)) and 90 ((g)-(i)). Here, the first, second and third columns represent the cooled, adiabatic and heated walls, respectively. The colors of the contour levels vary from -2.5 to 1, excluding the zero level (light to dark) for (a), from -1 to 1, excluding the zero level for (d) and from -3 to 6 for the rest.

heat sink here, as pointed out by Lechner et al. [22]. On the other hand, for the adiabatic and the heated cases, at the same y^+ location (figures 14b and 14c), the Q_3 is more dominant in comparison to the Q_1 which means that the cooled fluid moving towards the wall is the major contributor to the turbulent wall-normal heat-flux. Therefore, in these cases, the wall is acting as a heat source. In the buffer layer, $y^+ = 10$, the Q_3 is more dominant than the Q_1 irrespective of the wall temperature. From figures 14g-l, it can be seen that in the log region from $y^+ = 35$ to 90, the Q_1 is more dominant than the Q_3 for all of the cases highlighting that the principal contribution is coming from the events of the Q_1 than the events of the Q_3. From the observations drawn from this set of figures, it can be concluded that the wall-cooling has significant effect on the heat-transfer mechanisms for the compressible turbulent boundary layer which is clearly highlighted in the near-wall region (up to $y^+ = 5$). In the higher y^+ regions, the physical mechanisms responsible for the heat-transfer do not change significantly with the wall-temperature, but slight variations in their amplitudes are registered. This explains the difference in the levels of the wall-normal Reynolds heat-flux observed for the heated and the cooled walls found by Sharma et al. [29].

5. Conclusion

Direct numerical simulations (DNS) for the supersonic boundary layers (SBLs) with free-stream Mach number of $M_\infty = 2.2$ were carried out. Three DNS test cases were investigated in order to unravel the effects of the wall-temperature on the turbulent flow topology for the SBLs. The implications on the important physical parameters like the turbulent shear-stress, the orientation of the projections of the coherent structures in different planes, and different components of the turbulent heat-flux were analyzed using the joint probability density function (JPDF) distribution and the covariance integrands' analyses.

The results showed that the sweeps were the dominant physical phenomenon majorly contributing to the turbulent shear-stress in the buffer layer. But, for the heated wall, both the ejections and the sweeps became comparable transfer processes. In the log-region, ejections had the dominant contribution to the shear-stress irrespective of the wall-temperature. These trends showed similarities with the findings reported by Wallace et al. [8], Ong and Wallace [11] regarding the adiabatic incompressible boundary layers. The results presented also highlighted different trends for the angles of inclination (α and β) of the projections of the coherent structures in case of the heated wall, as a result of the increased heat transfer from the surface of the wall. The trends of α and β showed good agreement with the compressible and the incompressible counterparts reported in the literature.

The plots of the covariance integrands of the u' and T' showed that for the adiabatic and the heated walls, the Q_2 and Q_4 were the dominant quadrants implying the principal contribution of the fast moving cooled fluid towards the streamwise turbulent wall heat-transfer extending from the viscous sublayer to the log-region. Whereas for the cooled wall, the Q_1 and Q_3 were found to be the major contributors in the viscous sub-layer. A similar contrasting trend was observed for the cooled wall again, for the wall-normal component of the turbulent heat-flux in the viscous sub-layer where the Q_2 had dominance in comparison to the Q_4, meaning that heated fluid going towards the wall had more contribution towards the turbulent wall-normal heat-flux. For the rest, the Q_1 and Q_3 were the dominant quadrants.

6. Acknowledgements

This work was granted access to HPC resources of IDRIS under the allocation 2017-100752 made by GENCI (Grand Equipement National de Calcul Intensif- A0022A10103). The authors acknowledge the access to HPC resources of French regional computing center of Normandy named CRIANN (Centre Régional Informatique et d'Applications Numériques de Normandie) under the allocations 1998022 and 2017002. The funding resources provided from European projects entitled FEDER and NEPTUNE 1 are gratefully acknowledged. Authors would also like to extend their gratitude to both the reviewers whose critical comments helped us to substantially improve the quality of the paper.

7. References

[1] K. Bensayah, A. Hadjadj, A. Bounif, Heat transfer in turbulent boundary layers of conical and bell shaped rocket nozzles with complex wall temperature, Numerical Heat Transfer, Part A: Applications 66 (2014) 289–314.

[2] L. Duan, I. Beekman, M. Martin, Direct numerical simulation of hypersonic turbulent boundary layers. part 2. effect of wall temperature, Journal of Fluid Mechanics 655 (2010) 419–445.

[3] T. Theodorsen, Mechanisms of turbulence, in: Proceedings of the 2^{nd} Midwestern Conference on Fluid Mechanics, 1952.

[4] M. Head, P. Bandyopadhyay, New aspects of turbulent boundary-layer structure, Journal of fluid mechanics 107 (1981) 297–338.

[5] M. Stanislas, L. Perret, J.-M. Foucaut, Vortical structures in the turbulent boundary layer: a possible route to a universal representation, Journal of Fluid Mechanics 602 (2008) 327–382.

[6] X. Wu, P. Moin, Direct numerical simulation of turbulence in a nominally zero-pressure-gradient flat-plate boundary layer, Journal of Fluid Mechanics 630 (2009) 5–41.

[7] E. R. Corino, R. S. Brodkey, A visual investigation of the wall region in turbulent flow, Journal of Fluid Mechanics 37 (1969) 1–30.

[8] J. M. Wallace, H. Eckelmann, R. S. Brodkey, The wall region in turbulent shear flow, Journal of Fluid Mechanics 54 (1972) 39–48.

[9] J. M. Wallace, R. S. Brodkey, Reynolds stress and joint probability density distributions in the u-v plane of a turbulent channel flow, The Physics of Fluids 20 (1977) 351–355.

[10] W. Willmarth, S. Lu, Structure of the reynolds stress near the wall, Journal of Fluid Mechanics 55 (1972) 65–92.

[11] L. Ong, J. M. Wallace, Joint probability density analysis of the structure and dynamics of the vorticity field of a turbulent boundary layer, Journal of Fluid Mechanics 367 (1998) 291–328.

[12] A.-T. Le, G. N. Coleman, J. Kim, Near-wall turbulence structures in

three-dimensional boundary layers, International journal of heat and fluid flow 21 (2000) 480–488.

[13] P. Bechlars, R. Sandberg, Variation of enstrophy production and strain rotation relation in a turbulent boundary layer, Journal of Fluid Mechanics 812 (2017) 321–348.

[14] P. Bechlars, R. Sandberg, Evolution of the velocity gradient tensor invariant dynamics in a turbulent boundary layer, Journal of Fluid Mechanics 815 (2017) 223–242.

[15] E. F. Spina, A. J. Smits, S. K. Robinson, The physics of supersonic turbulent boundary layers, Annual Review of Fluid Mechanics 26 (1994) 287–319.

[16] M. V. Morkovin, Effects of compressibility on turbulent flows, Mécanique de la Turbulence 367 (1962) 380.

[17] A. J. Smits, J.-P. Dussauge, Turbulent shear layers in supersonic flow, Springer Science & Business Media, 2006.

[18] W. Li, L. Xi-Yun, Statistical analysis of coherent vortical structures in a supersonic turbulent boundary layer, Chinese Physics Letters 28 (2011) 034703.

[19] T. Maeder, N. A. Adams, L. Kleiser, Direct simulation of turbulent supersonic boundary layers by an extended temporal approach, Journal of Fluid Mechanics 429 (2001) 187–216.

[20] S. Pirozzoli, F. Grasso, T. Gatski, Direct numerical simulation and analysis of a spatially evolving supersonic turbulent boundary layer at M= 2.25, Physics of fluids 16 (2004) 530–545.

[21] S. Pirozzoli, M. Bernardini, F. Grasso, Characterization of coherent vortical structures in a supersonic turbulent boundary layer, Journal of Fluid Mechanics 613 (2008) 205–231.

[22] R. Lechner, J. r. Sesterhenn, R. Friedrich, Turbulent supersonic channel flow, Journal of Turbulence 2 (2001) 001–001.

[23] M. Shadloo, A. Hadjadj, F. Hussain, Statistical behavior of supersonic turbulent boundary layers with heat transfer at M_∞= 2, International Journal of Heat and Fluid Flow 53 (2015) 113–134.

[24] A. Trettel, J. Larsson, Mean velocity scaling for compressible wall turbulence with heat transfer, Physics of Fluids 28 (2016) 026102.

[25] A. Patel, B. J. Boersma, R. Pecnik, Scalar statistics in variable property turbulent channel flows, Physical Review Fluids 2 (2017) 084604.

[26] Y.-B. Chu, Y.-Q. Zhuang, X.-Y. Lu, Effect of wall temperature on hypersonic turbulent boundary layer, Journal of Turbulence 14 (2013) 37–57.

[27] M. S. Shadloo, A. Hadjadj, D. J. Bodony, F. Hussain, S. K. Lele, Effects of heat transfer on transitional states of supersonic boundary layers, in: Proceedings of Summer program, Center of Turbulence Research, Stanford University, USA, pp. 175–184.

[28] M. Shadloo, A. Hadjadj, Laminar-turbulent transition in supersonic boundary layers with surface heat transfer: A numerical study, Numerical Heat Transfer, Part A: Applications (2017) 1–14.

[29] S. Sharma, M. Shadloo, A. Hadjadj, Laminar-to-turbulent transition in supersonic boundary layer: Effects of initial perturbation and wall heat-transfer, Numerical Heat Transfer, Part A: Applications (2018) doi:10.1080/10407782.2018.1464785.

[30] A. Chaudhuri, A. Hadjadj, A. Chinnayya, S. Palerm, Numerical study of compressible mixing layers using high-order weno schemes, Journal of Scientific Computing 47 (2011) 170–197.

[31] G.-S. Jiang, C.-W. Shu, Efficient implementation of weighted eno schemes, Journal of computational physics 126 (1996) 202–228.

[32] A. Chaudhuri, A. Hadjadj, O. Sadot, E. Glazer, Computational study of shock-wave interaction with solid obstacles using immersed boundary methods, International Journal for Numerical Methods in Engineering 89 (2012) 975–990.

[33] D. Ngomo, A. Chaudhuri, A. Chinnayya, A. Hadjadj, Numerical study of shock propagation and attenuation in narrow tubes including friction and heat losses, Computers & Fluids 39 (2010) 1711–1721.

[34] O. Ben-Nasr, A. Hadjadj, A. Chaudhuri, M. Shadloo, Assessment of subgrid-scale modeling for large-eddy simulation of a spatially-evolving compressible turbulent boundary layer, Computers & Fluids (2016).

[35] L. M. Mack, Boundary-layer linear stability theory, Technical Report, CALIFORNIA INST OF TECH PASADENA JET PROPULSION LAB, 1984.

[36] F. M. White, I. Corfield, Viscous fluid flow, volume 3, McGraw-Hill New York, 2006.

[37] K. Masatsuka, I do like cfd, Published by Katate Masatsuka (2009).

[38] S. Sharma, M. S. Shadloo, A. Hadjadj, Laminar-to-turbulent transition in supersonic boundary layer: Effects of initial perturbation and wall heat transfer, Numerical Heat Transfer, Part A: Applications 73 (2018) 583–603.

[39] S. Sharma, M. Shadloo, A. Hadjadj, Effect of thermo-mechanical non-equilibrium on the onset of transition in supersonic boundary layers, Heat and Mass Transfer (2018) 1–13.